UNIVERSITY OF COPENHAGEN

MSc in Geophysics

Shallow Subsurface Imaging: A Geophysical Investigation using Integrated Methods

Insights into the geological structure of the northern Gulf of Aqaba through seismic imaging

Lana Župančić

Supervised by Mohammad Youssof and Klaus Mosegaard

March 2023

Lana Župančić
Shallow Subsurface Imaging: A Geophysical Investigation using Integrated Methods
MSc in Geophysics, March 2023
Supervisors: Mohammad Youssof and Klaus Mosegaard

University of Copenhagen
Niels Bohr Institute
Physics of Ice, Climate and Earth
Tagensvej 16
2200 Copenhagen N

Statement of Originality

This dissertation is submitted to the University of Copenhagen (Niels Bohr Institute) in fulfillment of the requirements of the degree of Master of Science.

This thesis represents my own original work toward this research degree and contains no material that has been previously submitted for a degree or diploma at this University or any other institution.

Lana Župančić
University of Copenhagen
March 12, 2023

Acknowledgments

My appreciation for my supervisor Mohammad Youssof and Sherif M. Hanafy's unfailing tolerance, excitement, in-depth expertise, and insightful input throughout my research is beyond words. Whenever I encountered a problem or had a query regarding my research or writing, their door was always open. Without them, I would not be able to go on this journey. Even though the meetings with Mohammad Youssof and Klaus Mosegaard were educational and helpful, their spectacular shared anecdotes were always the highlight of my day.

This thesis would not have been completed without their help and committed participation in each step of the procedure. I want to express my gratitude to you for your help and patience over the past year.

Also, I am appreciative of my friends and classmates' knowledge of overleaf editing, their late-night input on MATLAB code errors, and their encouraging study sessions.

I would be remiss in not mentioning my family for their moral support. My grandmother, aunt, and cousin, who offered their encouragement through phone calls. With my grandma's own brand of humor, she has been kind and supportive to me. My boyfriend's belief in me has kept my spirits and motivation high during this process. Lastly, big thanks to my boyfriend's dog for always being around me in literally every step of the way.

Abstract

This study investigates the subsurface structure of a valley located in the northern segment of the Gulf of Aqaba (Arabian Peninsula) using seismic records from advanced seismometers (ZLand types) with 3-component nodes and onboard GPS timing. A long 7.2-kilometer seismic profile is acquired perpendicular to the Gulf shoreline in the currently under-development NEOM city. The main purpose is to map the underlying faults and gauge the depth of the basement underneath this locality.

The multichannel analysis of surface waves (MASW) technique is used for the analysis of surface waves and uses the dispersion of surface waves for the determination of a 2D shear-wave profile. In this study, surface waves were generated through a seismic source, which is a 950 kg weight drop.

MASW is used to focus on the relatively shallow subsurface sedimentary succession and basement structure in this region. After applying a quality control and dispersion analysis to the dataset, a 2D shear-wave tomogram (SWT) is generated and compared to a P-wave velocity tomogram (PWT) from a recent study.

Both the SWT and the PWT show that the sediments are thicker on the western side of the tomogram and get thinner as you move toward the east. The PWT shows four faults, while they are not that visible on the shear-wave tomogram. On the other hand, disruptions of and around dispersion curves occurred around shot gathers where faults were anticipated (and imaged by PWT), which may represent a new clue for the presence of the fault system. These findings provide insights into the geological structure of the NEOM area and have implications for future seismic hazard assessments.

Contents

1 Introduction

The most significant earthquake hazard in the Arabian Peninsula is along the coast of the Gulf of Aqaba and near the Strait of Tiran (GAST). The hazard is due to earthquakes on the Dead Sea fault system, which extends from the Red Sea, through the Strait of Tiran, along the entire Gulf of Aqaba, and all the way north to Turkey. The fault system borders the north-moving Arabian plate and accommodates primarily left-lateral transform motion.

Many devastating earthquakes have occurred on the Dead Sea fault during the past 2000 years, with the last major recorded earthquake occurring in the middle of the Gulf of Aqaba in 1995 (Mw 7.3), causing several fatalities and considerable damage in Nuweiba in Egypt and Haql in Saudi Arabia. The earthquake released only a portion of the moment that has accumulated in the GAST area during the past several hundred years, so more major earthquakes can be expected in the future.

A similar-sized earthquake on the next fault segment to the north would cause extensive damage in the populated cities of Taba (Egypt), Aqaba (Jordan), and Haql (Saudi Arabia), while a large earthquake to the south would threaten the tourist towns of Sharm El-Sheikh in Egypt and Maqna in Saudi Arabia. The recent decision to build a bridge between Saudi Arabia and Egypt, the King Salman Bridge, in addition to establishing NEOM City has put this area in focus. The planned bridge will span the Strait of Tiran and go across the Dead Sea fault, which is capable of producing magnitude > Mw 7 earthquakes, multi-meter fault offsets, and violent shaking.

The Dead Sea fault system in the GAST area is trans-tensional, meaning that along with the transform motion, significant normal faulting takes place with subsidence within the gulf and uplift of the coastal ranges on both sides. These vertical motions have led to the dramatic topography of the area, with >1.8 km deep basins within the gulf and almost 2 km high mountains bounding it.

The fault system has 3–4 en echelon fault segments within the gulf that bound three major pull-apart basins. Only one of these segments ruptured in the 1995 earthquake, while the other segments have not ruptured for several centuries. The 1995 earthquake likely increased the stress on the adjacent fault segments, bringing them closer to failure. However, as the geometry and location of these fault segments are not fully known, such a statement is difficult to support. Better information about the active faults and their geometry within the gulf is needed, both for assessing the potential size and influence of future earthquakes and the likely interaction between fault segments.

In this project, we intend to start to improve our knowledge of the location and geometry of active faults in the GAST region and its overall tectonics, as well as obtain new information about how frequent and how large major earthquakes in the area are likely. The newly acquired high-resolution multi-beam bathymetric data of the Gulf for fault mapping, aided by re-analysis of earthquake data, and with sampling and dating uplifted coral terraces to constrain the activity of normal faults as well as carry out an active seismic survey to gain insights into the structure of these faults.

The whole large project is to re-measure a geodetic GPS network to constrain moment accumulation rates, collect sediment cores from the seafloor for evidence of prehistoric earthquakes, and run scenario calculations to estimate expected shaking levels. These activities will help better understand the active processes taking place in the gulf, provide information about the location and structure of faults in the area, and reveal how fast stresses are accumulating on them. Together, the integrated results of our seismic studies would greatly improve our knowledge of the active tectonics in the region and provide valuable information about the seismic hazard.

Theoretical background

2

2.1 Surface Wave Inversion

Surface wave (SW) inversion using high-frequency seismic data is a technique used to extract information about the Earth's subsurface structure. This method is particularly useful for determining the shear-wave velocity (Vs) profile, which is an important parameter for geotechnical engineering and earthquake hazard assessment. This kind of seismic wave propagates along the Earth's surface and is characterized by its particle motion being perpendicular to the direction of wave propagation. The two main types of surface waves are Love waves, which have a horizontal Particle motion, and Rayleigh waves, which have both horizontal and vertical particle motion.

High-frequency seismic data refers to recordings with a frequency range that is roughly up to 50 Hz. These frequencies correspond to wavelengths that are sensitive to the depth of investigation required for geotechnical and earthquake engineering applications. SW inversion involves extracting the dispersion curves, which are the relationship between phase velocity and frequency for different modes of surface waves. These dispersion curves can be obtained using various techniques, such as the multichannel analysis of surface waves (MASW) or the spectral analysis of surface waves (SASW).

Using a significantly smaller depth range of examination, the multichannel analysis of surface waves (MASW) approach deals with surface waves at lower frequencies (for example, 1-30 Hz) (Park *et al.*, 2007). The fundamental tenet is that the deeper the penetration, the lower the frequency (i.e., the longer wavelength) (this is why, in near-surface applications, we need 4.5 Hz geophones). Density and VP are mostly irrelevant for surface-wave propagation, which is primarily dependent on VS and layer thickness. A 3-component (3C)

geophone can be utilized if we need to study deeper levels (that cannot be perceived through the analysis of the surface waves collected with typical, relatively short arrays) (Dal Moro, 2020).

The surface wave in a layered medium has a phase velocity that varies with frequency instead of a single velocity. The dispersion curve is the relationship between frequency and phase velocity. While at lower frequency values the influence of deeper layers becomes more and more dominant, the phase velocity tends asymptotically to the Rayleigh velocity of the material in the deepest layer, the phase velocity is the Rayleigh velocity of the material in the uppermost layer at higher frequency values. In MASW, the dispersive nature of Rayleigh waves is used to map the subsurface shear wave velocities (Vs) (Kesarwani *et al.*, 2012).

Once the dispersion curves are obtained, they are used to invert the Vs profile using various inversion techniques, such as the genetic algorithm or the neighborhood algorithm. The resulting Vs profile can be used to estimate other geotechnical parameters, such as the soil's shear modulus and damping ratio.

The background theory behind this technique is explained by the relationship between Vs structure of the subsurface and the dispersion behavior of surface waves that have been described by Love's equation and Rayleigh's equation, which relate the phase velocity of surface waves to the shear wave velocity structure of the subsurface. Love's equation describes the relationship between the phase velocity of Love waves and the shear wave velocity structure of the subsurface. Love waves have their motion of particles perpendicular to the direction of wave propagation. They are dispersive, which means that their phase velocity depends on the frequency of the wave.

Love's equation is given by:
$v = \frac{\sqrt{\frac{\mu}{\rho}}}{\sqrt{\kappa^2 - h^2}}$

where v is the phase velocity of the Love wave, μ is the shear modulus of the subsurface, ρ is the density of the subsurface, k is the wave number $(2\pi/\lambda)$ where λ is the wavelength of the Love wave, and h is the depth of the shear wave source.

The term represents the shear wave velocity (Vs), which is the velocity of shear waves in the subsurface. This equation shows that the phase velocity of Love waves is related to the shear wave velocity structure of the subsurface, as well as the wavelength of the Love wave and the depth of the shear wave source. By measuring the phase velocity of Love waves for a range of frequencies, it is possible to invert the shear wave velocity structure of the subsurface.

Similarly, Rayleigh's equation describes the relationship between the phase velocity of Rayleigh waves and the shear wave velocity structure of the subsurface. Rayleigh waves are characterized by the motion of particles that are both perpendicular and parallel to the direction of wave propagation. Rayleigh waves are also dispersive, and their phase velocity depends on the frequency of the wave. Rayleigh's equation is given by:

$$v = \frac{\sqrt{\frac{\mu}{\rho}}}{\sqrt{\kappa^2 - 0.25h^2}}$$

where v is the phase velocity of the Rayleigh wave, μ is the shear modulus of the subsurface, ρ is the density of the subsurface, κ is the wave number ($2\pi/\lambda$) where λ is the wavelength of the Rayleigh wave, and h is the depth of the shear wave source.

Like Love's equation, the term represents the shear wave velocity (Vs). Rayleigh's equation shows that the phase velocity of Rayleigh waves is related to the shear wave velocity structure of the subsurface, as well as the wavelength of the Rayleigh wave and the depth of the shear wave source. By measuring the phase velocity of Rayleigh waves for a range of frequencies, it is possible to invert the shear wave velocity structure of the subsurface.

In summary, Love's equation and Rayleigh's equation are fundamental to SW inversion using such kind of seismic data. By relating the phase velocity of surface waves to the shear wave velocity structure of the subsurface, these equations provide a means of determining the subsurface structure. The resulting shear wave velocity profile can then be used to estimate other geotechnical parameters, such as the soil's shear modulus and damping ratio, which are important for geotechnical and earthquake engineering applications.

In conclusion, SW inversion using high-frequency seismic data is a powerful tool for determining the subsurface structure of the Earth, particularly for

geotechnical and earthquake engineering applications. This technique is based on the dispersion of surface waves, and the resulting Vs profile can provide valuable information for understanding the Earth's subsurface properties.

2.2 Active and Passive dataset

Active sources are most advantageous for seismic tomography since we are confident of the precise time and location of both the source and receiver. A variety of techniques are used to collect active data from human-made seismic sources, including chemical reactions, the dropping of masses, airgun rounds, explosions, etc. The ability to record seismic waves in any place is the fundamental benefit of using active sources. Active sources frequently provide extensive information about the crust's shallower levels. Unfortunately, because they can only be created close to the surface, the resolution in depth is limited (Alejandro Díaz-Moreno *et al.*, 2016).

In the active dataset, wavefields produced by natural sources were regarded as background noise. The response of natural sources will be the main topic of the passive dataset. These sources could be found anywhere on the surface or beneath the ground (Berkhout and Verschuur, 2011).

These data are produced over a large depth range, which typically results in improved ray coverage in the analyzed region. Clear P- and S-waves are typically produced by local and regional seismicity, which are then inverted to give convincing velocity models and source characteristics (Alejandro Díaz-Moreno *et al.*, 2016).

2.2.1 Field Trip Overview

Using seismic data from advanced seismometers (ZLand kinds with 3-component nodes and onboard GPS timing), the region of interest is situated in a valley in the northern part of the Gulf of Aqaba (Arabian Peninsula) (figure 2.1). 120 3-component wireless nodes are used to record field data, and each node is buried inside a small hole to improve the coupling with the ground. The orientation and level of each node are the same. The distance between nodes is 60

m, resulting in a 7.2 km overall profile length (Sherif M. Hanafy, Mohammad Youssof, *et al.*, 2020).

In the fieldwork, Sherif Hanafy and Mohammad Youssof (2020) recorded two datasets:

- Active dataset where they used 450 kg accelerated weight drop as a seismic source. As there were 120 nodes, due to mechanical problems with the weight drop, they recorded the first 100 shot gathers. The shot gathers next to nodes 101 to 120 were not recorded. To increase the signal-to-noise ratio (SNR) of recorded data, a total of 10 stacks were fired at each location.

- Passive dataset where for 32 days, the nodes were left in the location to continuously record ambient noise.

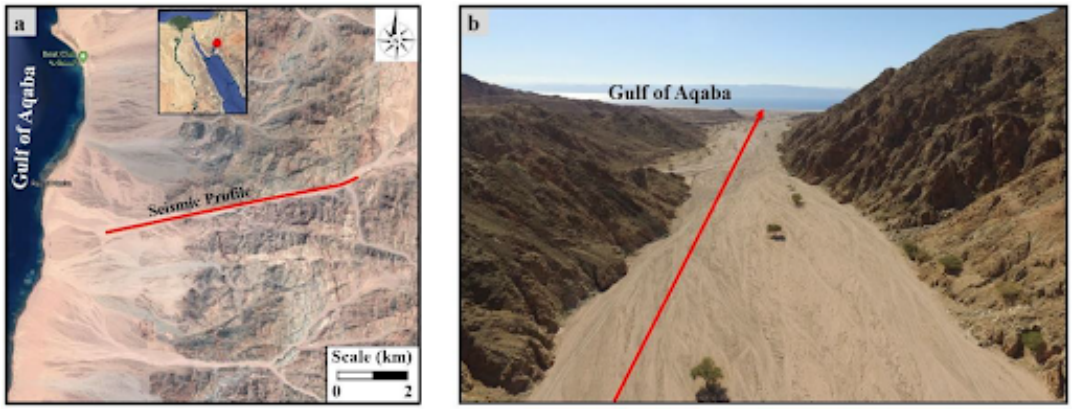

Figure 2.1.: A 7.2-kilometer seismic profile where the location of the research area is shown by the red dot in the inner frame of (a). A zoomed-in view of the research region can be seen in (a), while the image in (b) is an aerial photo acquired by a drone while looking west. The seismic profile's location is indicated by the red lines in (a) and (b) (Hanafy, 2019).

3 Exploration of data

3.1 Investigation of Passive Data

Investigation of the passive, also called ambient data, has been done in a program called MATLAB. Due to the 3-component nodes used in the field trip, raw data will be presented in that way (Figure 3.1). One of the reasons for having three different components is to see better wave propagation, for example in Z component is better for visualizing P-wave and Rayleigh-wave studies (Dal Moro, 2020).

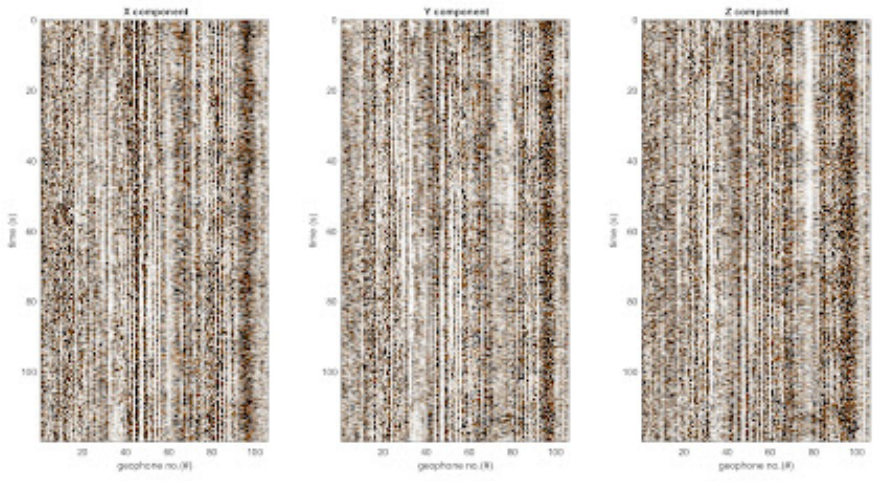

Figure 3.1.: Different subplots represent X, Y, and Z components with the Number of Geophones on the x-axis and Time (s) on the y-axis.

Another way of viewing it is by frequency spectrum, but for a better overview of it, only Z-component will be chosen for a discussion (Figure 3.2).

The frequency spectrum can be divided into two segments:

- The first peak represents ambient noise where the peak usually occurs at 6.81Hz while the whole noise can be counted up to 50Hz. Ambient noise

as such is excited by random fluctuations near and below the surface and can be considered a natural seismic source (Yang and Ritzwoller, 2008; Hanafy, 2021).

- The second part, which is usually counted from 82Hz - 222Hz, is considered high-frequency noise and can be easily removed from data by a band-pass filter.

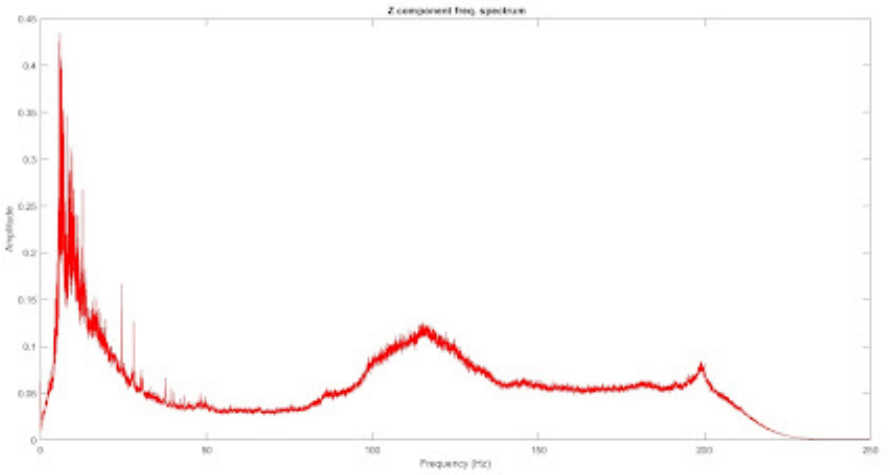

Figure 3.2.: Z-component frequency spectrum of passive data with a frequency on an x-axis and amplitude on a y-axis.

3.2 Effect of input data on the inverted velocity model

As a previous investigation, this one will be also made in the same program but with a different method. This time, we will be focusing on the active dataset which will be used to generate SWT. The observation is done in three steps:

1. Dispersion curve picking
2. Analysis of two created figures
3. Quality control

These 3 steps have been done in 5 trials where the 5th one is final and used for inversion to generate SWT. For the first three trials, 80 out of 100 shot gathers, while in the fourth and fifth, all 100 shot gathers have been picked.

3.2.1 First Trial

The main goal of this trial is to understand the data and in what way do pickings influence the modeling results. The trials as a whole process can lead to be improved modeling improvements to get the best tomogram possible. One of the main things is to understand which frequency range will be the most beneficial and which shot gather range should be used. In this trial, we will focus on comparing correct and wrong picking. To see with what we are working with, we started with a frequency range [1 100] and chose shot gather number 42 as an example (Figure 3.3).

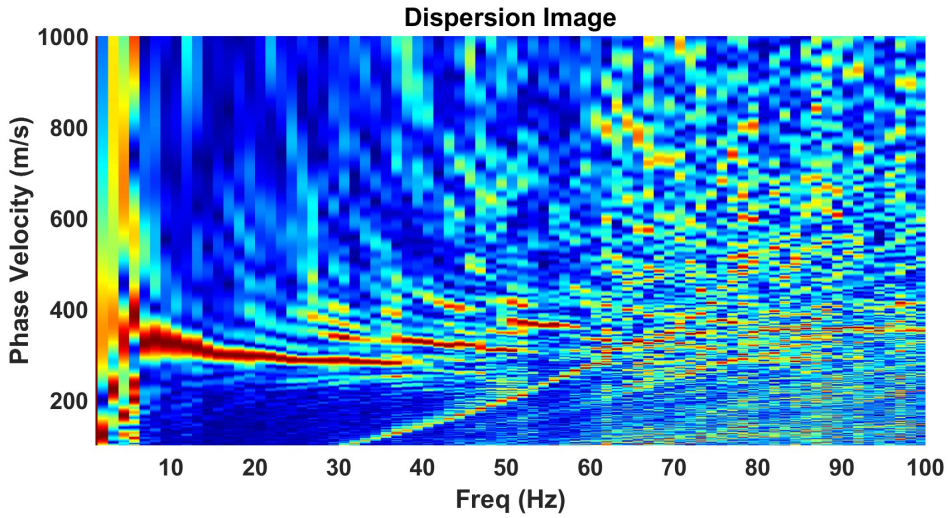

Figure 3.3.: First image of dispersion curve for shot gather number 42 with frequency range [1 100] before picking.

As can be observed, the dispersion curve continues up to 40Hz, after which there is only noise. We have been using all 120 traces, which is often not a good idea, and that is one of the reasons why. We will only allow 40 traces (nearly 100m) from the selected shot gather since surface waves go a great distance from the surface. In order to have a stronger dispersion curve, we will only select shot gathers from 42:82 when selecting the dispersion curve for shot gather number 42. The dispersion curve will readily change if the put restriction is not followed and a random selection is made, leading to incorrect pickings and outcomes. The frequency range [1 81] is selected for our first trial (figure 3.4). Figure A.1 illustrates the primary codes used to accomplish this (codes were written and modified by (Sherif M. Hanafy, Jing Li, *et al.*, 2020)).

In figure 3.4, the upper image named a) represents the random shot gather range and we will call it wrong picking. It can be seen that the dispersion curve looks much stronger, but on the other hand, it looks much different than the lower figure named b) (correct picking) and figure 3.3. It can be easily picked from 1Hz, and even though a noise starts around 57Hz, it can be picked all the way to 81Hz. Correct picking resembles figure 3.3 and a dispersion curve stops around 43Hz, and it is not safe to pick after that. Noise also starts from around 57Hz and there is no point in keeping it. The black line represents our picking line. Moreover, to avoid bad pickings, we need to pay attention to a picking line. In the diversion, we don't like any kind of sharp discontinuity and that is why we will use spline interpolation which will make the picking line smooth.

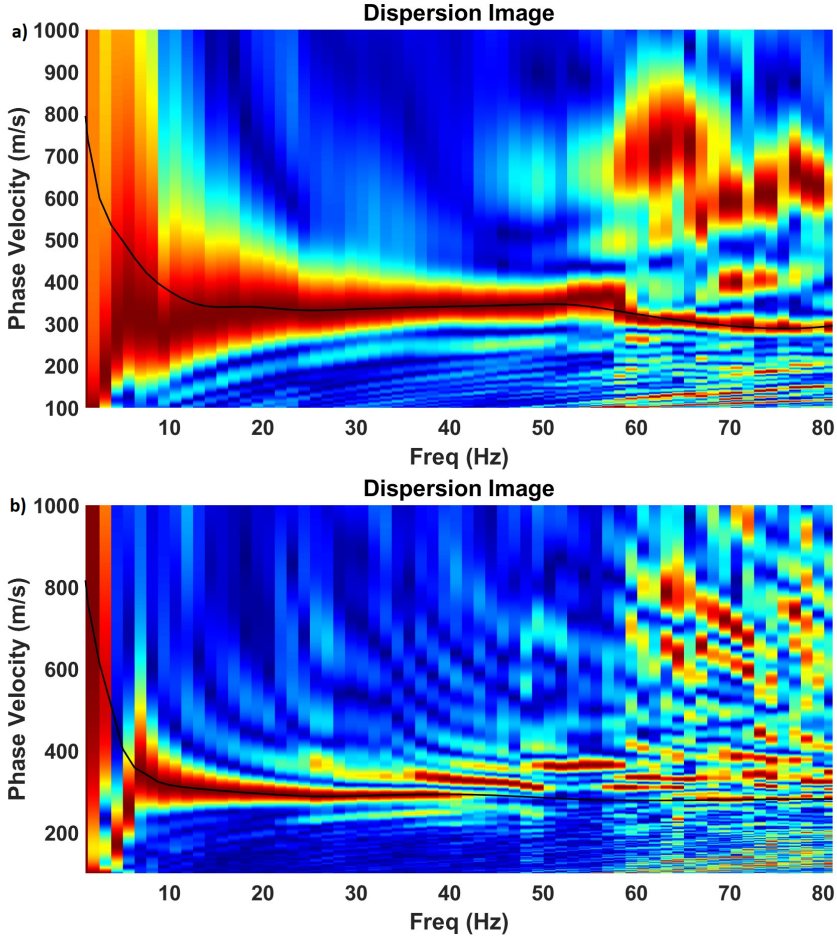

Figure 3.4.: Difference between a shot gather limitation. We are still looking at the shot gather number 42, but in figure a) a shot gather range is chosen randomly (wrong picking) while in figure b) it is chosen for exactly 42:82 (correct picking). The black line represents our picked dispersion curve.

When the dispersion curve has been picked, the second part of the observation is in order which is the analysis of two figures:

1. Comparison of Dispersion Curve
2. Model Test for SW Dispersion Inversion

First to analyze is a comparison of the dispersion curve and we are using it only for reference. There are 3 models - true mode, initial model, and inverted result. The true model is represented as blue dots and it represents our pickings. Red dots are the initial guess and black dots represent the inverted result. Our goal is to focus on the conversion between blue (the true model) and black (the inverted result) and see how close they are to each other. Moreover, what the code is trying to do is that it is trying to find the smoothest curve that can fit our picking. The smoother we are in the beginning, the better results we will get.

It can be seen how the wrong, a) figure and correct picking b) figure have similar results (figure 3.5). Both of the pickings started between a velocity of 700-800 m/s and ended around a velocity of 290 m/s. They couldn't converge in the first 10-15Hz, while wrong picking also had some troubles from 40-81Hz. We can say that correct picking converged better and smoother.

Model test for SW dispersion inversion is an important part of our exploration. This time we are looking at velocities that are shown with 2 lines - the initial model, the red line, and the inverted result, the black line (figure 3.6). Information saved in MATLAB for the inverted result will be used in the third step for quality control. Moreover, depth also has a big role in this. The maximum depth gotten during picking, taken wrong picking, for example, is 1140.5 meters where we are not trusting all that. We are thrusting only 1/8 of the maximum depth which is 142.56 meters and it is immediately uploaded in the model test.

There is no significant difference in the test models for both pickings. The biggest difference is in the behavior of the result in the first 20 meters. Both of the model test velocities started around 235 m/s and ended around 685-700 m/s with a depth of 140-150 meters.

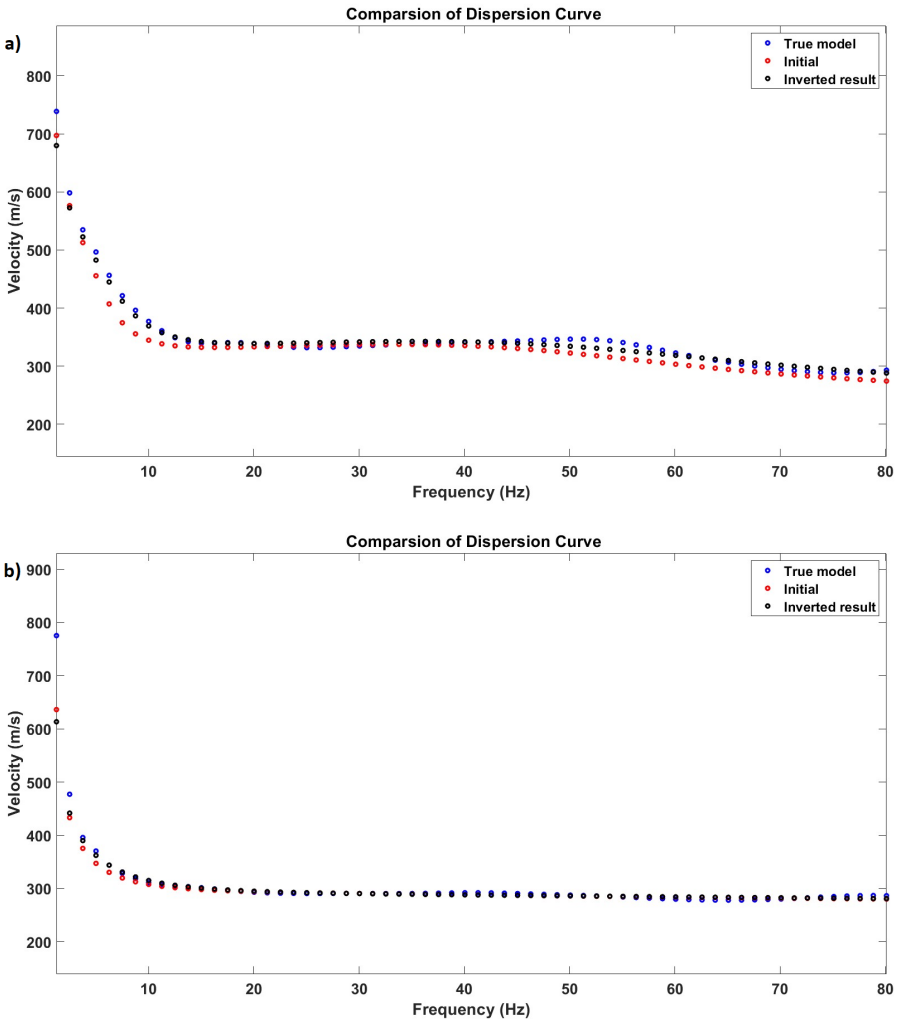

Figure 3.5.: Comparison of dispersion curves where a) is for a shot gather range randomly chosen while a figure b) it is chosen for exactly 42:82.

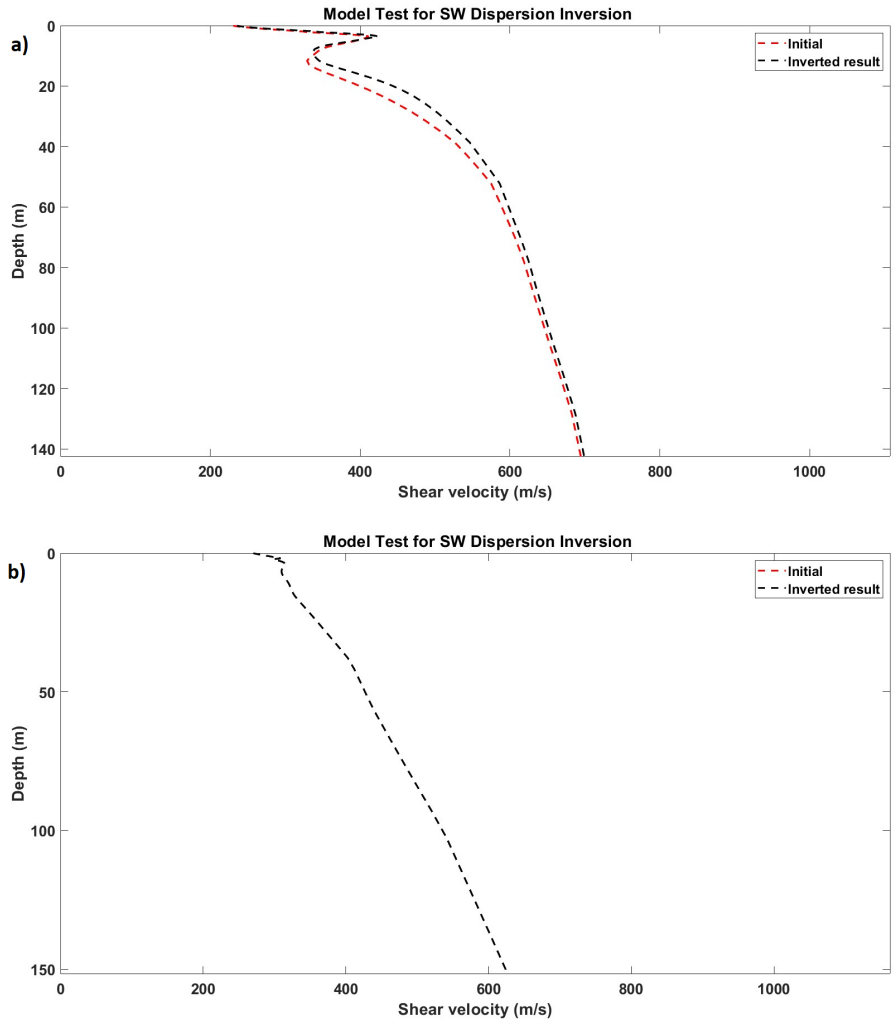

Figure 3.6.: Model test for SW dispersion inversion where a) is for a shot gather range randomly chosen while a figure b) it is chosen for exactly 42:82.

The last step in the first analysis is quality control. When the dispersion curves were picked for 80 shot gathers, we got almost the same result so we chose the result from the wrong pickings.

Quality control (figure 3.7) represents the interpolated velocities for each shot gather. Starting point is picking a region that is starting with a first shot and ending at the last shot. We will divide this region into equal distances in both directions (vertical and horizontal). In vertical it is every 5 meters. We will use these values and interpolate between them to have a velocity at the intersection of the vertical location which is the location of the shot and use it every 5 meters. That step is done for all of the shot gathers. The velocity that is used is the same velocity that is in the model test as an inverted result (black line). The used distance in the horizontal direction is 60 meters which is the distance between shot gathers. Moreover, the maximum depth for the model is 100m.

Quality control can also be called a 2D velocity model. We are looking to have a smooth transition between the shot gathers. The ones that are standing out with being too strong as shot gather number 36 or being too weak shot gather number 18 have to be reprocessed as picked again. The other way of viewing the change in velocities for all picked dispersion curves is by plotting all of them (figure 3.8). It provides the clearest picture of the range and degree of velocity variation for each selected dispersion curve. Moreover, 100 meters was chosen as the maximum depth, which is the same as for the 2D velocity model. The codes used for generating this 2D model can be seen in figure A.2.

SWT will perform better the narrower the velocity range. The gradual increase in velocities is depicted in this graphic. At 0 meters, the beginning velocity ranges from 200 to 350 m/s, while at 100 meters, the maximum velocity ranges from 470 to 770 m/s. It demonstrates that there is a 300 m/s velocity difference. We can see that velocities, which are very slightly knotted, do not exhibit the "pattern" up to a distance of 10 meters. Some of them are acting like they are going to a peak, some of them are going straight down, while for some of them, we cannot describe them precisely. Afterward, at 10 meters, all of them have the same pattern as they are gradually increasing with depth.

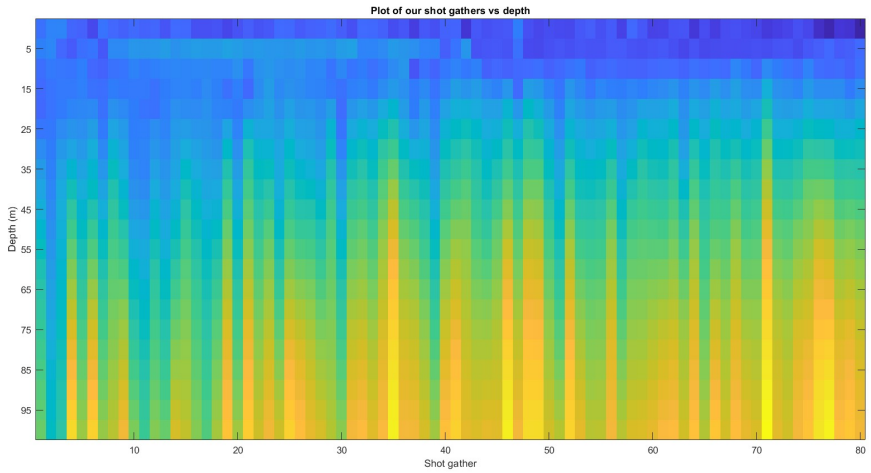

Figure 3.7.: Quality control for the first trial.

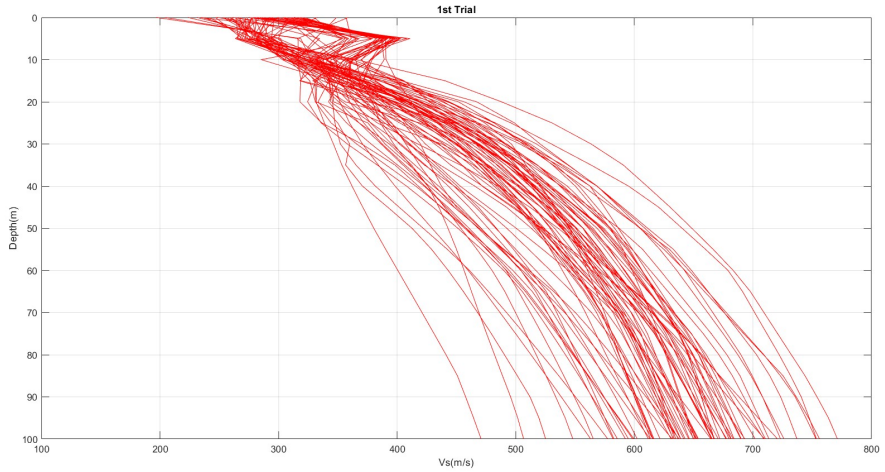

Figure 3.8.: All 80 shear velocities plotted from the first trial with a depth (m) of 100 meters on the y-axis and shear velocity up to 800 m/s (Vs (m/s)) on the x-axis.

This trial is mostly for a learning experience and it will not be inverted to an SWT. As the frequency range [1 81] was too big, it caught too much unnecessary noise so we will continue with a smaller frequency range. To get a proper range, we will focus on the correct type of picking and see which range can catch all dispersion curves the best.

3.2.2 Second and Third Trial

For further investigation, we chose [1 48] for a second trial and [5 45] for a third trial. The reason for choosing two different frequency ranges is to see if these points will make a difference in quality control:

- The first 4-5Hz was always hard to pick as it was more of a guess than an actual certainty
- Starting picking from a lower phase velocity in the third trial

In the second trial, the best way to pick was to start from a phase velocity around 800 m/s, but as there is no specific way to pick, it was picked blindly and what seems the best (figure 3.9). In the third trial, the only where we were unsure in the pickings was at 5Hz, while everywhere else it was very easy to pick. The above dispersion curves in both trials are the first order that is not included in pickings. The dispersion curve is the fundamental model that goes all the way to the end.

The true model and inverted result successfully converge in both trials and the shape of the curves is very similar (figure 3.10). Both of them have the same problem at the beginning of the frequencies which is up to 15-18Hz, but the rest converged nicely.

Model tests, on the other hand, are very different (figure 3.11). The second trial's model resembles the first trial's model - starting shear velocity point is around 268.8 m/s and the ending is around 703.3 m/s with a corresponding depth of 142.5 meters. The third trial model doesn't have that big velocity difference between starting and ending points which are 289.6 m/s and 340 m/s. Moreover, we can see that the trusting depth is 7 times smaller and it is 21.2 meters.

2D velocity models are also different (figure 3.12). The quality has improved from the first trial but it still has room for an upgrade. Shot gathers with a much stronger yellow color occurred more in the second trial as we were starting pickings from higher phase velocities, while in the third trial yellow color seems much smoother and there are not so many irregularities as there are in the second trial. One more difference is the first 15 shot gathers where

they are stronger and yellow in a), while they are bluer in b). As a third trial seems more fluent, we will invert the results for an SWT.

Even if on the 2D velocity models we can see the improvement, when we plot all velocities together from the second and the third trial, we see another story (figure 3.13). For both trials, the starting velocity at 0 meters can be divided into two sets which are showing the same velocity patterns up to a maximum of 20 meters - one is with a velocity range from 199 - 304 m/s while the other is from 323 - 383 m/s.

Velocities colored in red, represent the second trial and it can be seen how it does not differ that much from the first trial. Velocities have almost the same pattern, they are still gradually increasing and their difference is less for 54 m/s. On the other hand, velocities colored in blue are the third trial. While they are also increasing with depth, they are not increasing as much as they did in the second trial. In other words, we got smaller velocities. On the other hand, the velocities difference is much bigger (307 - 641 m/s) which is 334 m/s.

Even though the 2D velocity model shows better results in the third trial, here the second trial is much better due to the smaller velocity difference. The best way to continue is with the characteristics of the third trial. We will keep the same frequency range but we will focus more on finding the right balance in the pickings so the 2D velocity model gives even better results.

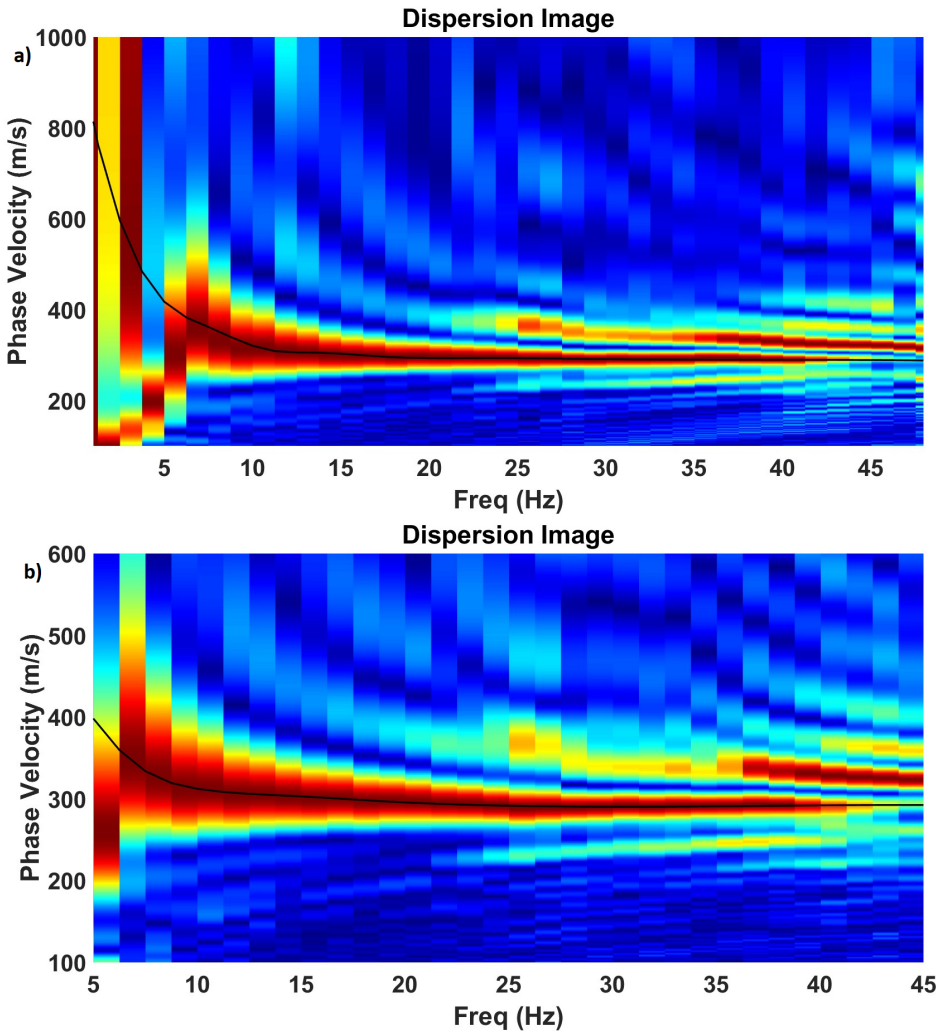

Figure 3.9.: Dispersion images of picked dispersion curves for a second trial in a) with a [1 48] frequency range, and for a third trial in b) with a [5 45] frequency range.

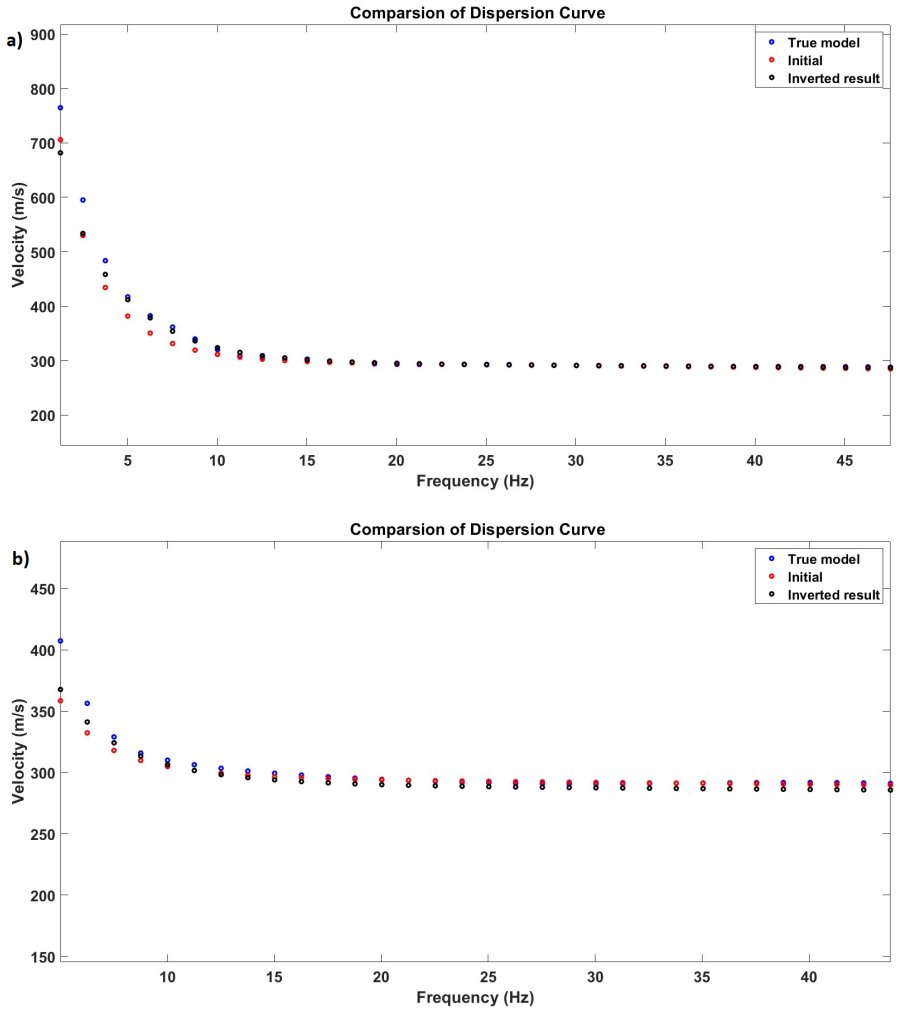

Figure 3.10.: Comparison of dispersion curves for a second trial in a) and for a third trial in b).

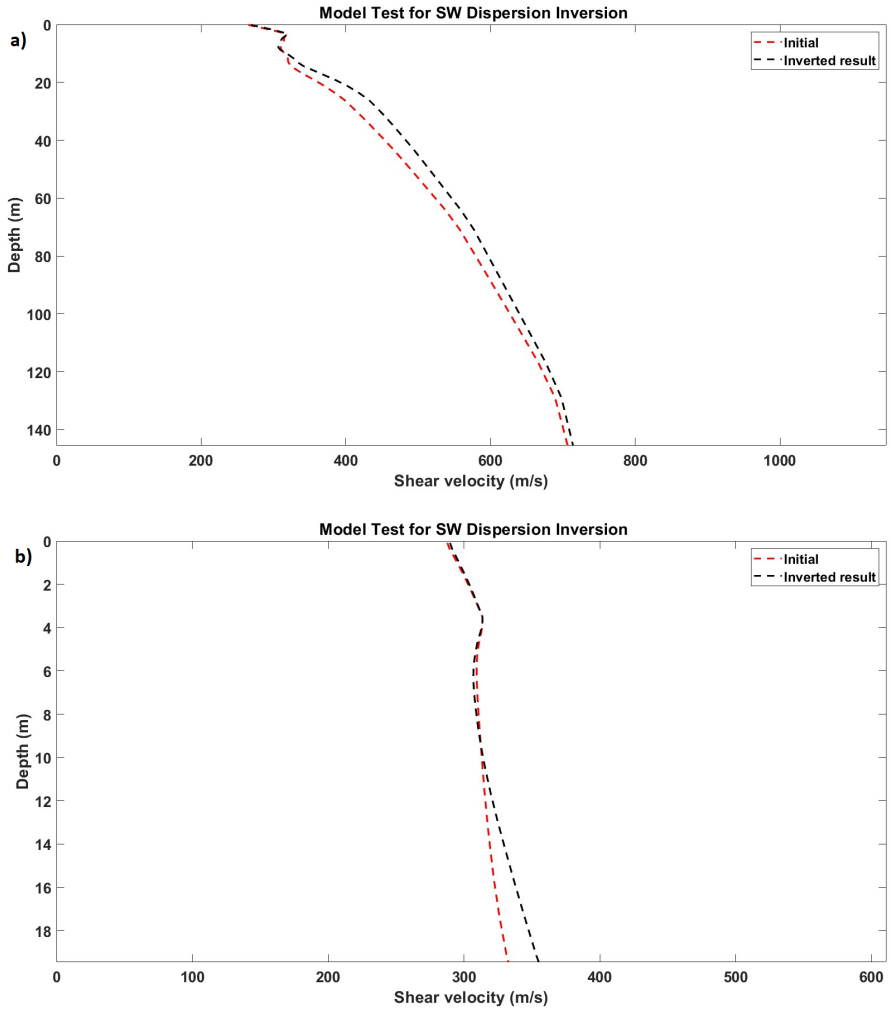

Figure 3.11.: Model test for SW dispersion inversion with the depth (m) on the y-axis and shear velocity (m/s) on the x-axis for the second trial a) and the third trial b).

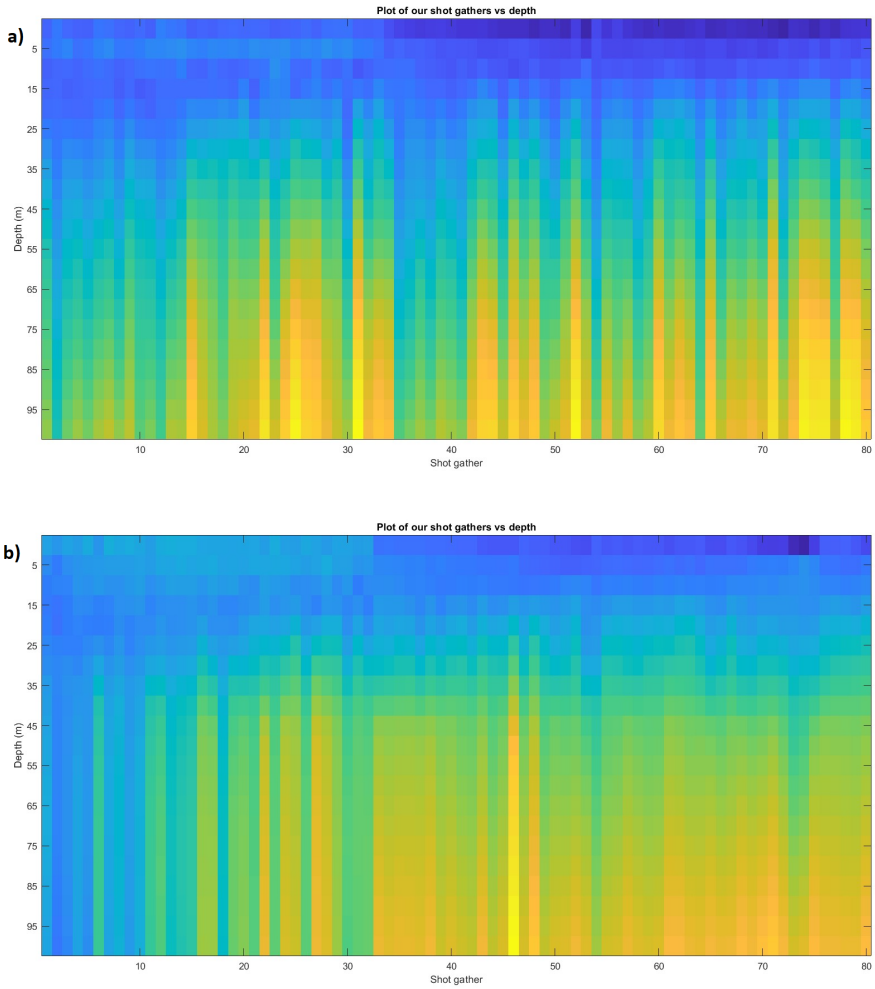

Figure 3.12.: Quality control for 80 shot gathers with depth (m) on the y-axis, and the number of shot gathers on the x-axis for the second trial a), and the third trial b).

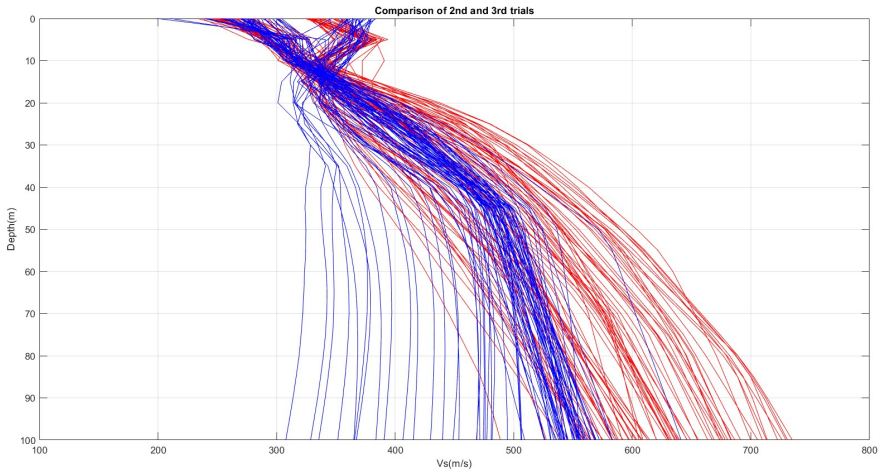

Figure 3.13.: Comparison of the 160 velocities with a maximum depth of 100 meters from which 80 velocities colored in red represent the second trial while the other 80 velocities colored in blue represent a third trial.

3.2.3 Fourth and Fifth Trial

For the fourth trial, we have been focusing on perfecting dispersion curve pickings, and this time, instead of 80 shot gathers, we picked dispersion curves for all 100 shot gathers. Specifically, we have focused on an overlap between the true model and the inverted result (figure 3.14 b)) which resulted in a better 2D velocity model (figure 3.15 a)). It looks much smoother and there are not so many significant outstanding between the interpolated velocities. As picking all over again is not necessary, we can improve the model in two ways - reprocessing or removing shot gathers. Both of the improvements will be based on averaging the picking that stands out the most with the velocities that it is standing next to it. Let us take a shot gather number 99 as an example. We will look at the velocities in the shot gathers 98 and 100 and what we can do is:

- Reprocess the picked dispersion curve. The easiest way to do it is to see what the real issue is to see the figures of comparison of dispersion curves for the shot gathers 98 and 100 and try to pick the curve that resembles the most both pickings. Most of the time the beginning of the picking is an issue and it has to be (in this example), started from a bigger phase velocity than the last time.
- Remove the velocity values. What that means is not to remove it completely as it will cause the problem in the offside direction. It means removing the velocities from the manual (our) picking, and do the averaging of velocities from the shot gathers 98 and 100. As in that way it will not be our picking, it is advised to do a maximum of 10% like that. In this report, none of them are done in this way, but it was one of the possibilities.

Even if not all of the pickings were changed, making a new 2D velocity model is called the fifth trial. It has been focused on reprocessing the picked dispersion curves while still paying attention on the overlapping true model and inverted results. The model has improved a lot as there are no outstandings and the transition between inverted velocities seems much smoother (figure 3.15 b)). As both of the 2D velocity models are good, we will invert both of them to SWT and see what reprocessing has changed and how much it improved the SWT.

Moreover, the other velocity model has also improved (figure 3.16). For both trials, the initial velocities at 0 meters go from 243 - 374 m/s. Velocities are increasing much faster from 20 to 50 meters than in the last couple of trials, but around 100 m they do not differ much. In the fourth trial (red), the Vs range at 100 meters is from 498 - 623 m/s where the difference is, unlike in the other trials, only 125 m/s. While the fifth trial gives the best results where Vs differs only 54m/s (542 - 596 m/s).

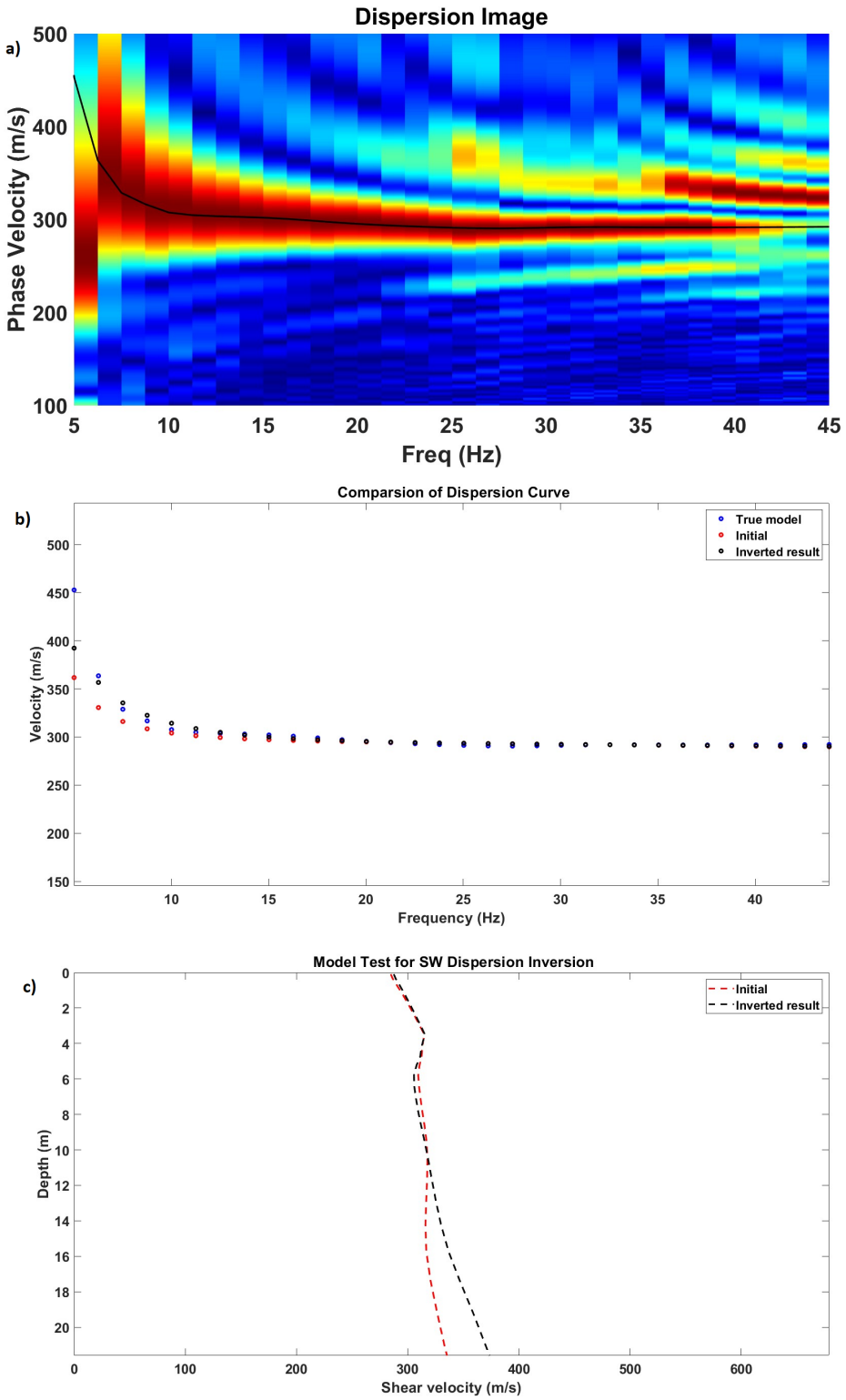

Figure 3.14.: Fourth trial for a shot gather number 42 in a frequency range [5 45] represented with a dispersion image a), comparison of dispersion curve b) and model test for SW dispersion inversion c).

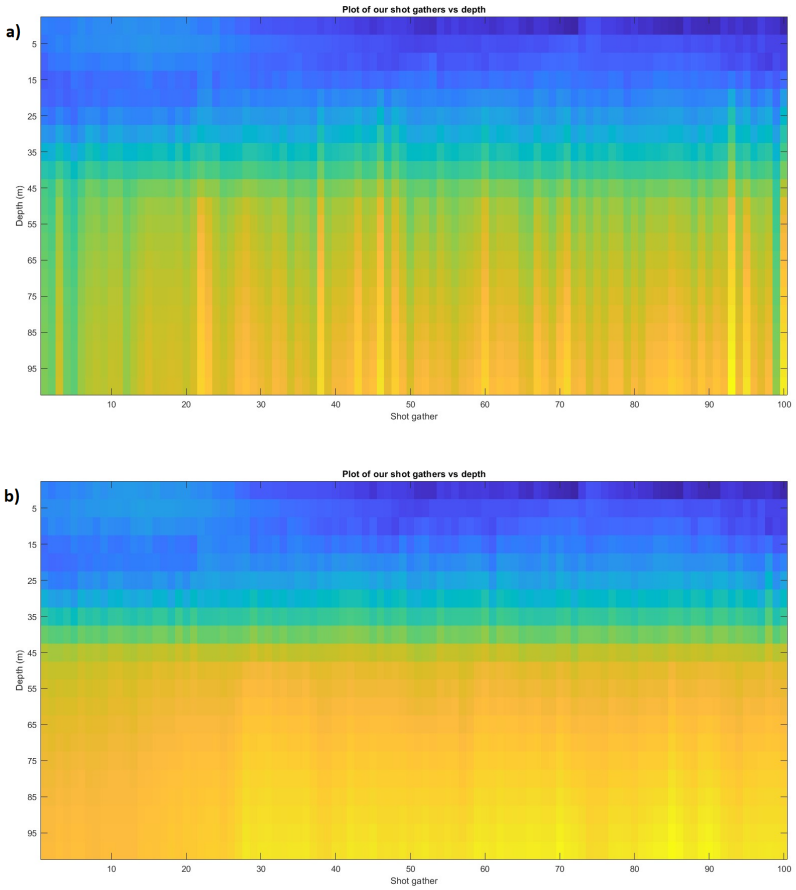

Figure 3.15.: A 2D velocity model with depth (m) on the y-axis and the number of the shot gathers on the x-axis for the fourth trial a), and the fifth trial b).

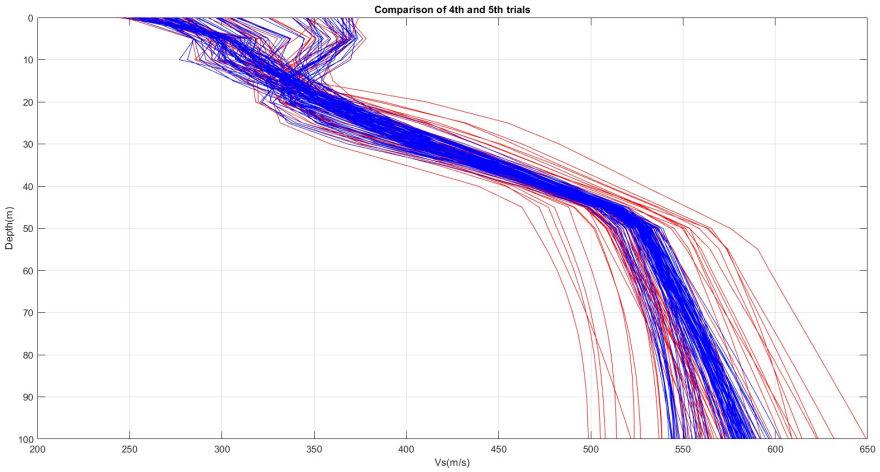

Figure 3.16.: Comparison of the 200 velocities with a maximum depth of 100 meters from which 100 velocities colored in red represent the second fourth while the other 100 velocities colored in blue represent a fifth trial.

3.3 Dispersion curve disruptions

The frequency range is set in a way that the dispersion curve can be followed from the beginning till the end, which is in this case from 5 can be characterized as the beginning and 45Hz can be characterized as the end. During this exploration, some changes in the dispersion curve model have been noticed. Changes have been characterized as

- Disruption of the whole dispersion curve (figure 3.17, the left column) where dispersion starts splitting in the middle. It results in a smaller dispersion curve where during the following shot gathers it becomes bigger and takes it looks almost the same as it was in the beginning, while the cut part becomes the higher order and it disappears or becomes not that noticeable over time.

- The end of the dispersion curve exhibits signs of splitting (figure 3.17, the right column). It would seem like the ending is becoming a higher order as in the previously explained scenario, but it merges again with the dispersion curve. Moreover, the noise, which is usually after 50Hz, starts from 35Hz, but it disappears as soon as the split part merges with the dispersion curve.

If we imagine that the described disruptions can be imagined as one cycle, we have noted 5 of them (table 1). As the distance between shot gathers is 60 meters, every shot gather is multiplied by 60 to see at what distance on the profile it will maybe occur. Later on, we will see if they will have some influence on the SWT tomogram or if they can mean something else.

Table 3.1.: Disruption in the dispersion curves was noted in 5 cycles.

	Shot gather range	Distance (m)
1	21 - 31	1260 - 1860
2	52 - 56	3120 - 3360
3	71 - 83	4260 - 4980
4	88 - 91	5280 - 5460
5	94 - 100	5640 - 6000

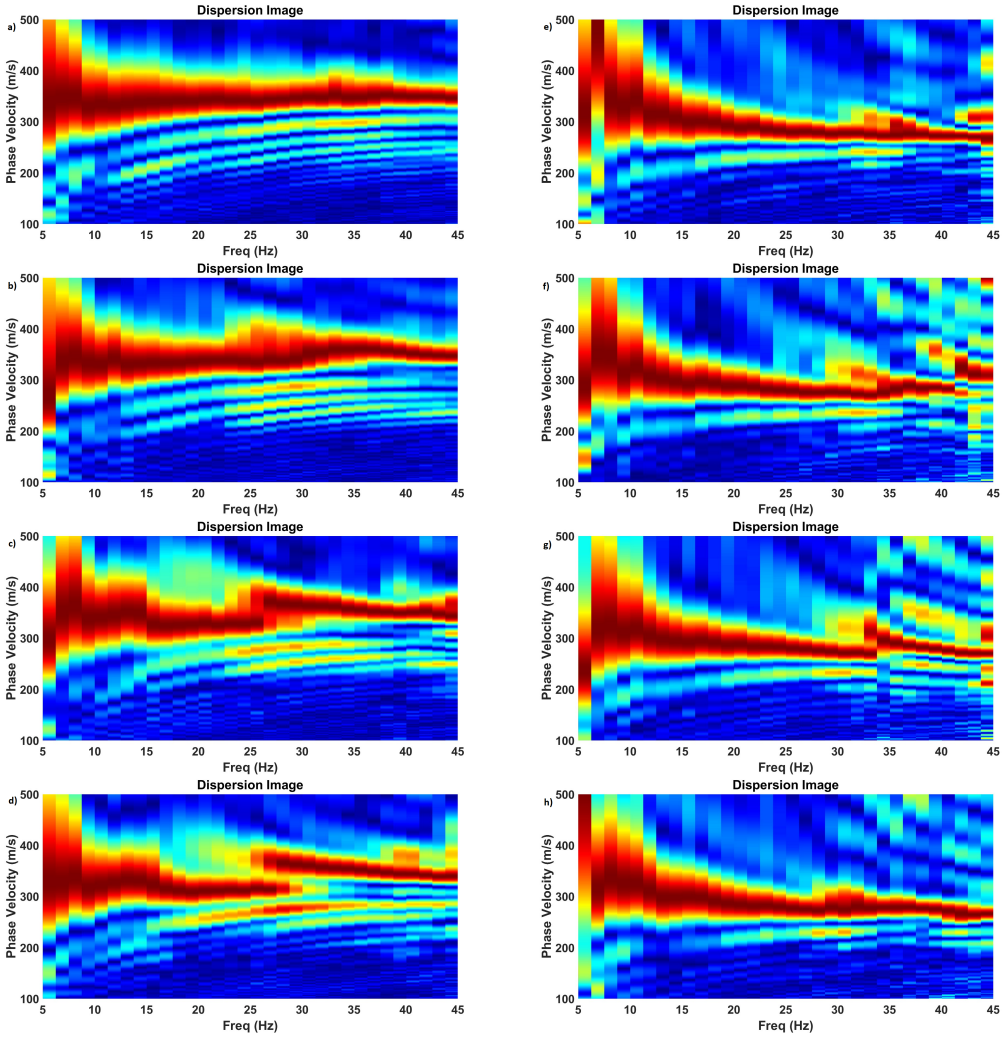

Figure 3.17.: Changes in the dispersion curve, where the column on the left assigned with letters a), b), c), and d) correspond to shot gathers 21, 24, 27, 31 while the column on the right with letters e), f), g), and h) correspond to shot gathers 88, 89, 90 and 91.

4 Geology of the study area

The Dead Sea (Levant) left-lateral transform fault ends at the Gulf of Aqaba at its southernmost point. From the Red Sea, via the Gulf of Aqaba, and north through the Dead Sea, Lebanon, and Syria, this about 1000 km long fault system represents the western boundary of the Arabian plate (Hanafy *et al.*, 2014). Moreover, it links the Zagros zone of continental collision with the Red Sea, where sea-floor spreading takes place (figure 4.1) (Ben-Avraham *et al.*, 1979).

The Gulf of Aqaba is one of particular relevance since it is one of only two locations where a mid-ocean ridge system transforms into a transform system and runs into a continent. The other location is the Gulf of California. The Gulf itself is the most striking of the significant morpho-tectonic depressions that run over the majority of its length. Another rift formation that emerges from the Red Sea is the Gulf of Suez rift (Ben-Avraham *et al.*, 1979).

Around 180 km long and 25 km wide, the Gulf of Aqaba is created by a series of three primary fault segments that define pull-apart basins. These basins' normal faults permit some extension in addition to the dominant strike-slip motion, resulting in an abrupt topography (Hartman *et al.*, 2014). Faults are the primary structural component of the Gulf of Aqaba and are a result of rifting and continental breakup (Ben-Avraham *et al.*, 1979).

On both sides of the Gulf of Aqaba, sediments from the younger phase of rifting, primarily of terrestrial origin (alluvium, lake, and playa beds), are common but relatively thin. These indicate that the marginal faults are no longer active because they overlap them. These faults, which are somewhat farther from the shores of the Gulf, were created during the first stage of rifting (Ben-Avraham *et al.*, 1979).

AL-Tanni et al. (2014) explain how the basement is unconformably overlain by 2 different kinds of sediment formation (figure 4.2). Two sedimentary layers above the basement are Wadi-sediments (silt and sand deposits) and carbonate rocks (Hartman *et al.*, 2014; Hanafy, 2019). As a result, layers of sediments with various grain sizes and porosities characterize the internal heterogeneity (Hartman *et al.*, 2014). As can be observed, quaternary deposits predominate in the region of our study, both on the surface and in the valleys between basement rocks.

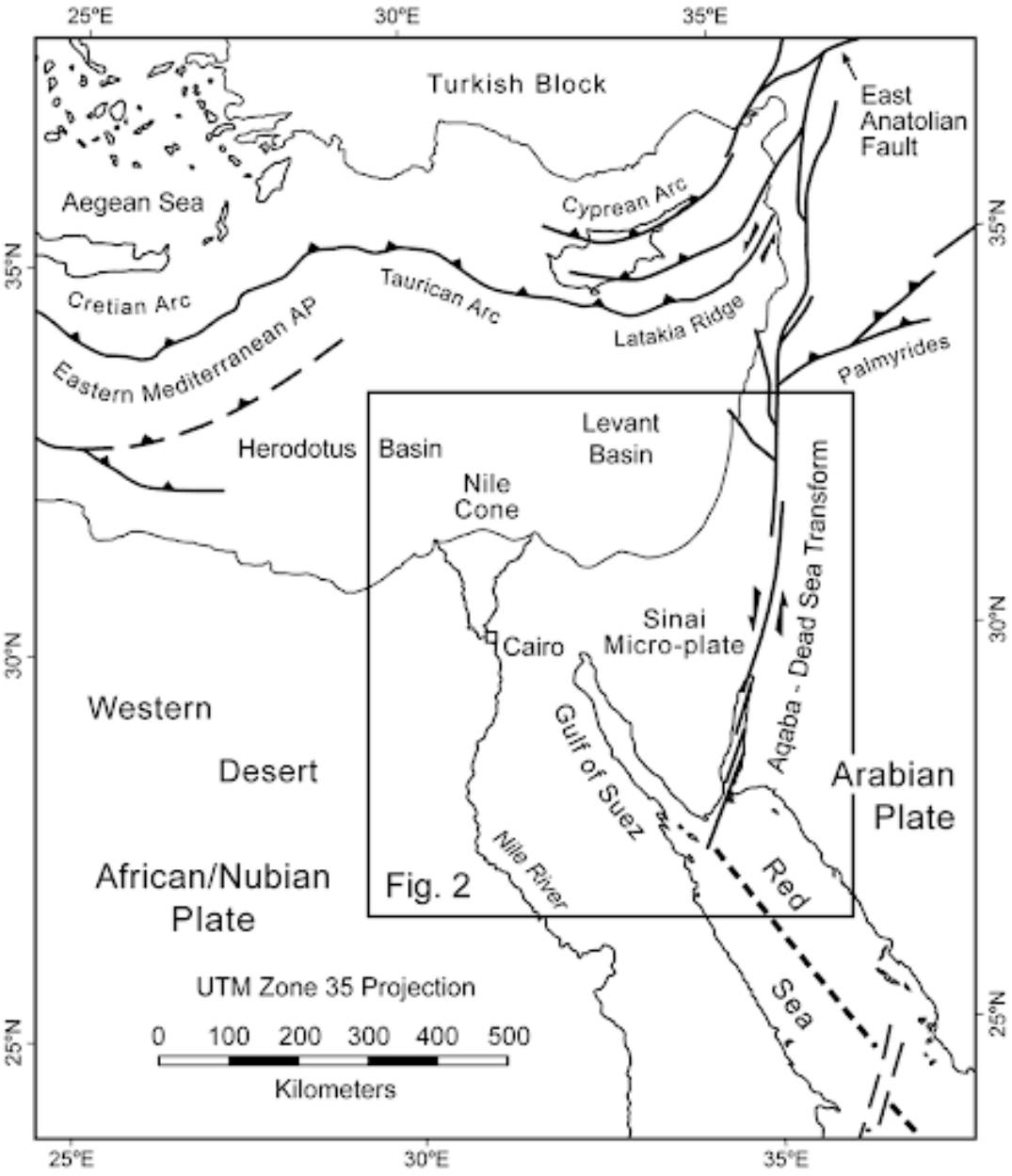

Figure 4.1.: The Gulf of Aqaba and the Dead Sea transform fault's tectonic setting. Bold lines indicate plate boundaries (Bosworth *et al.*, 2017).

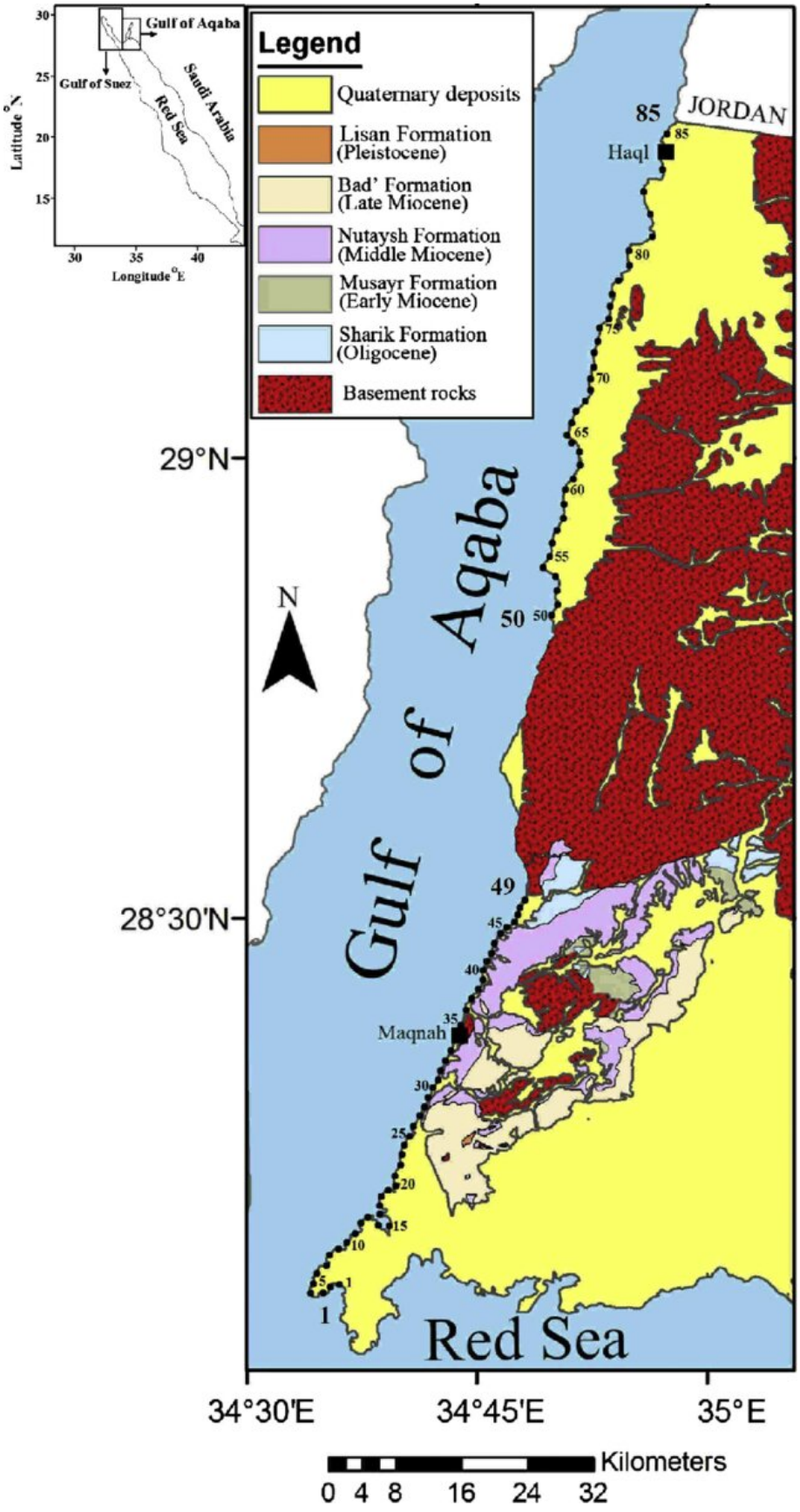

Figure 4.2.: The geologic outcrop of the Gulf of Aqaba (Al-Taani *et al.*, 2014). The black dots represent their sampling sites. Our profile location is placed between sampling sites 60 and 65.

5 Previous Work on the Study Area

A primary motivation for this work was a previous study that was made on the same site. The active data, unlike in this project, was used for picking the first break travel times which are then inverted for generating the P-wave velocity tomogram (PWT) (Hanafy, 2021). The same PWT will be compared to our SWT. Additionally, 32 days of recorded ambient (passive) data were converted to 120 virtual common shot gathers that show the behavior of surface waves (Hanafy, 2021).

5.1 P-wave velocity tomogram

In the fieldwork, 10 stacks were fired at each shot location during the recording of an active data set to increase a signal-to-noise ratio (SNR). As the SNR of recorded data was too low and it can be a major obstacle in picking the first arrivals, to enhance it, a two-stage iterative super virtual refraction interferometry was used (ISVI) (Hanafy, 2021). With applying a bandpass filter with parameters 1, 5, 60, 85 Hz (Hanafy, 2021), first arrivals for only around 1km, but with 2-stage ISVI we could get more offsets and it can be expanded for 3-4km from the shot location (Figure 5.1) which provided better imaging of the surface and deeper imaging (Hanafy, 2022).

As ISVI helped with enhancing the SNR at far offset traces, the first arrival travel times of almost 70% of the traces were able to be picked (Hanafy, 2019) and inverted to generate a PWT (Figure 5.2) (Hanafy, 2021). Y-axis can be ignored. It assumes that the highest point is 0, while 0 should be at the start of the tomogram on the left (west) side and everything underneath should be negative. On the other hand, it shows the correct elevation difference between the west and east (right) sides (Hanafy, 2022) and the correct thicknesses of the layers.

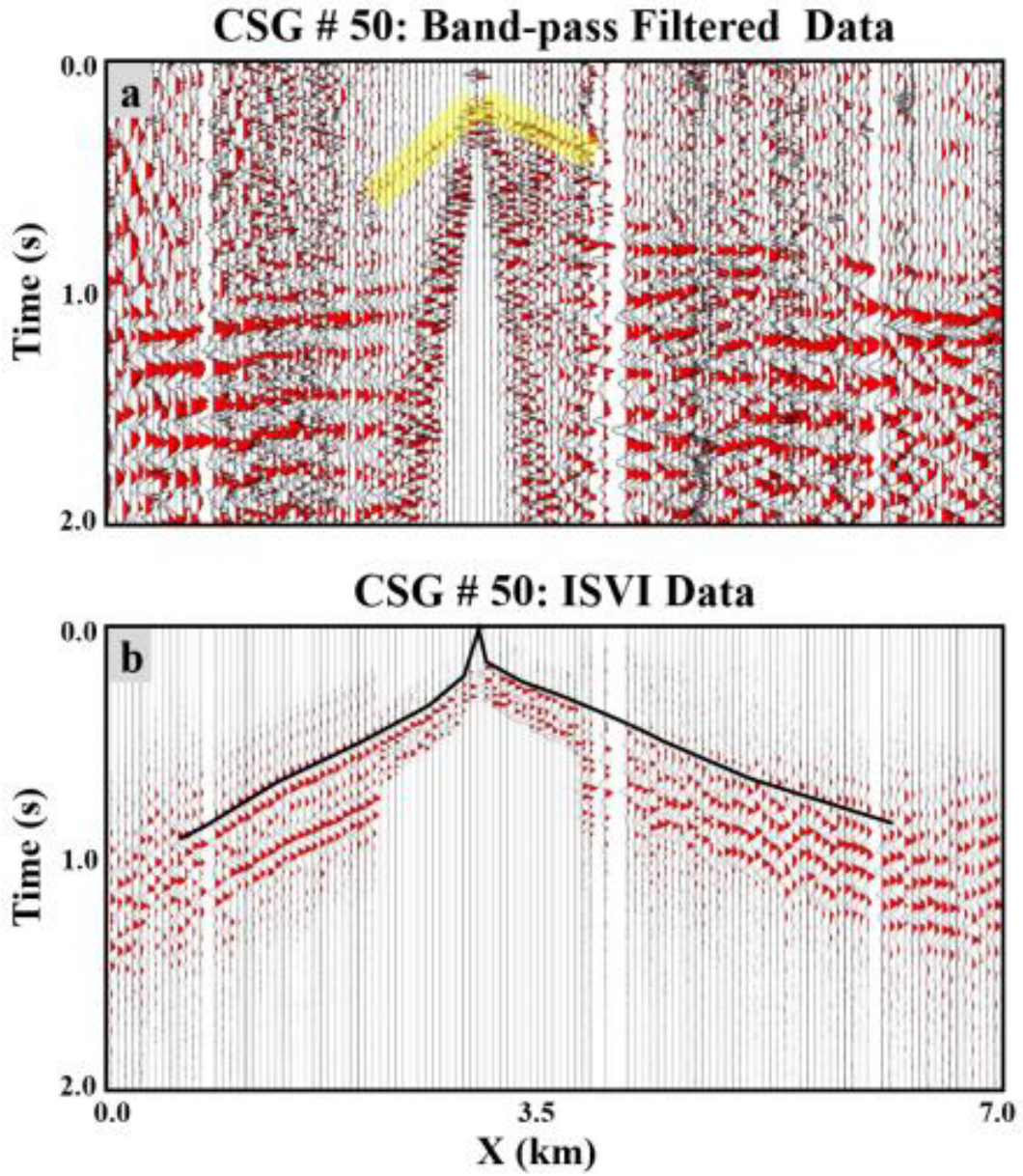

Figure 5.1.: Hanafy, 2021 chose shot gather number 50 as an example. Traces after the band-pass filter are shown in an (a) figure and the yellow highlighted zone represents the first arrival times, while the same traces after the 2-stage ISVI are shown in a (b) figure, with this time black line that represents the first arrival times.

PWT can be simplified into two layers separated by the black line. There are several layers, but for simplicity, all sedimentary part is the first upper layer, and the basement, igneous rock, is the second lower layer (Hanafy, 2022). The sedimentary layer, with a velocity range of 400 - 2500 m/s, is very thick (up to 500m) on the west side and it is slowly decreasing when we go to the east side of the profile leaving us with less than 30m. A basement layer, with a

velocity higher than 4500 m/s, also experiences thickening from the west side (300m) to the eastern side (30-50m) (Hanafy, 2019).

While looking at the basement layer, 4 normal faults (F1, F2, F3, and F4) can be seen. Faults F1, F2, and F4 are dipping toward the western side, while F3 is dipping toward the eastern side. (Hanafy, 2019) If there is no need to have a surface map confirmation about the faults, the satellite image has been checked and fault F2 can be nicely seen (Figure 5.3). It is a very sharp discontinuity between the basement on the surface (mountains, east side), and sedimentary on the surface (west side). Moreover, F1 can be seen, while F3 and F4 cannot on the satellite image (Hanafy, 2022).

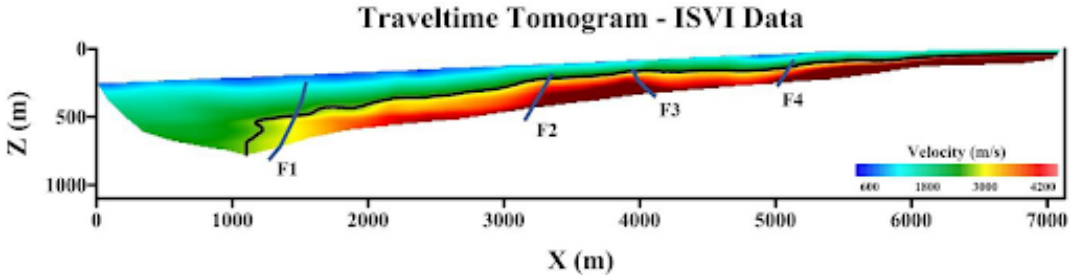

Figure 5.2.: The P-wave traveltime tomogram of the 2-stage ISVI where the black line divides the tomogram into two layers, and thick blue lines represent possible faults (Hanafy, 2021).

Figure 5.3.: Satellite image and confirmation of Faults F1 and F2, while F3 and F4 cannot be seen (Hanafy, 2022).

5.2 A virtual shot gather

Using cross-correlation interferometry, 120 virtual common shot gathers are gathered from the recorded ambient data (Hanafy, 2021). Virtual CGS number 41 is picked and compared to PWT to show the accuracy of the 1D surface wave inversion and the behavior of the surface waves (Figures 5.4) (Hanafy, 2021; Hanafy, 2022).

It was noticed that surface waves have deeper penetration until reaching fault F2 where their behavior is completely different and there is only a small amount of surface waves. Hanafy, 2021 hypothesis is that the thickness of the sediment layer, on the west side of fault F2 is thick enough to generate stronger surface waves, while the absence of surface waves on the east side of fault F2, is due to the low thickness of the sediments overlay the bedrock due to subsurface faulting.

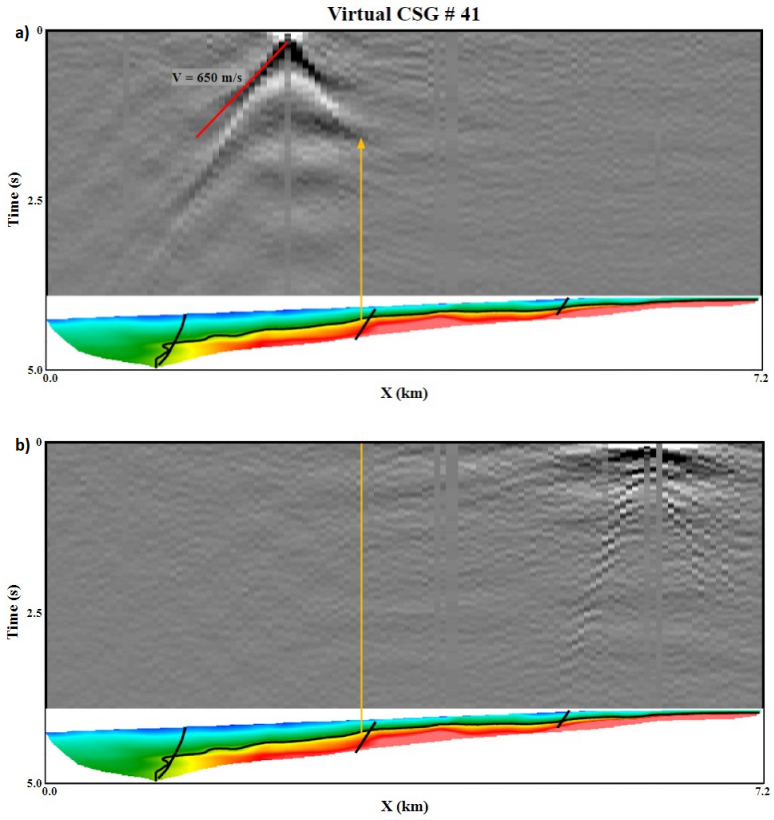

Figure 5.4.: Virtual common shot gather for number 41 showing a) surface waves having deep penetration while after a fault showing in b) they have changed the whole behavior and the penetration is not that significant as it is mostly focused near the surface.

6 Processing and inversion of dataset

We will concentrate on the study of the SWT models generated by the Surfer program. The SWT model's progress over the previous three trials will be examined first, and the best model will be selected for comparison with the PWT.

6.1 Third Trial

The first SWT model that we chose to generate is from the third trial (figure 6.1). The west is on the left side while the east is on the right side. The Y-axis can be disregarded since it implies that the surface begins at 300 meters on the west, but in reality, it should be at zero, and everything below should be negative because it is below the surface. Due to selecting dispersion curves from 80 of 100 shot gathers, offset (m) displays 5000 meters. The range of shear velocity is 150 to 1050 m/s.

One of the biggest problems with this SWT is the velocity anomalies. The majority of them happen before 2000 meters, where velocities quickly increase from 150–200 m/s to 550 m/s. The 2D velocity model showed the same abrupt velocity shifts (figure 4.10). We cannot have sudden velocity shifts in geology. Moreover, we cannot accurately interpret anything from this SWT, thus we won't use it in our discussion.

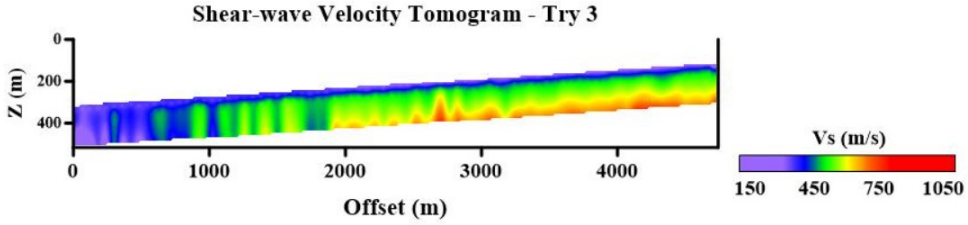

Figure 6.1.: Generated SWT model from the third trial.

6.2 Fourth and Fifth Trial

As the third trial wasn't that promising, the fourth and fifth trials show a completely different picture (figure 6.2). The west is on the left side while the east is on the right side. Y-axis will be ignored also in these SWTs; it assumes that the highest point is 0. on the left, it should start from 0, then on the right, it should be positive, and everything underneath should be negative. On the other hand, it shows the correct elevation difference between the west and east sides and the correct thicknesses of the layers. The difference between the left and right is around 300m which is an elevation difference.

For both of the trials, agree on the same look with minor differences. The range of shear velocities is different from the third trial, which is from 240 m/s to 640 m/s. There are no sudden velocity changes and figures are much easier to read. The shear-wave velocity tomogram shows 4 layers:

- The topmost layer is characterized by a shear velocity (Vs) of <310 m/s. The thickness of a layer is gradually decreasing from the west (70m) to the east (<10m).
- The second layer has a Vs of 310 - 410 m/s whose thickness also gradually decreases from the west (110m) to the east (50m).
- The third layer has a Vs of 410 - 590 m/s whose thickness gradually increases from the west (50m) to the east (120m)
- The fourth layer has a Vs of >590 m/s and it is gradually increasing from west to the east (30m). This layer is described from the fifth trial as from the fourth is hard to say correctly.

For simplicity, we will divide the SWT into two main layers and we can have a shear velocity of 410 m/s as a divider. Everything above 410 m/s is a sedimentary layer, while everything below is the basement which is igneous rock. The sedimentary layer in both trials, looking at the west is thick around 110 meters, and it continuously gets shallower going to the east where it is thick only 50 meters. The basement we have some differences. In the fourth trial, we have some small velocity anomalies up to 800 meters (offset-wise). Moreover, shear velocities higher than 590 m/s are not consistent as in the fifth trial, they are going more up and down. Due to small differences, we will

choose the SWT model generated from the fifth trial. The fifth trial is smoother and clearer, and it will be better for comparison with PWT.

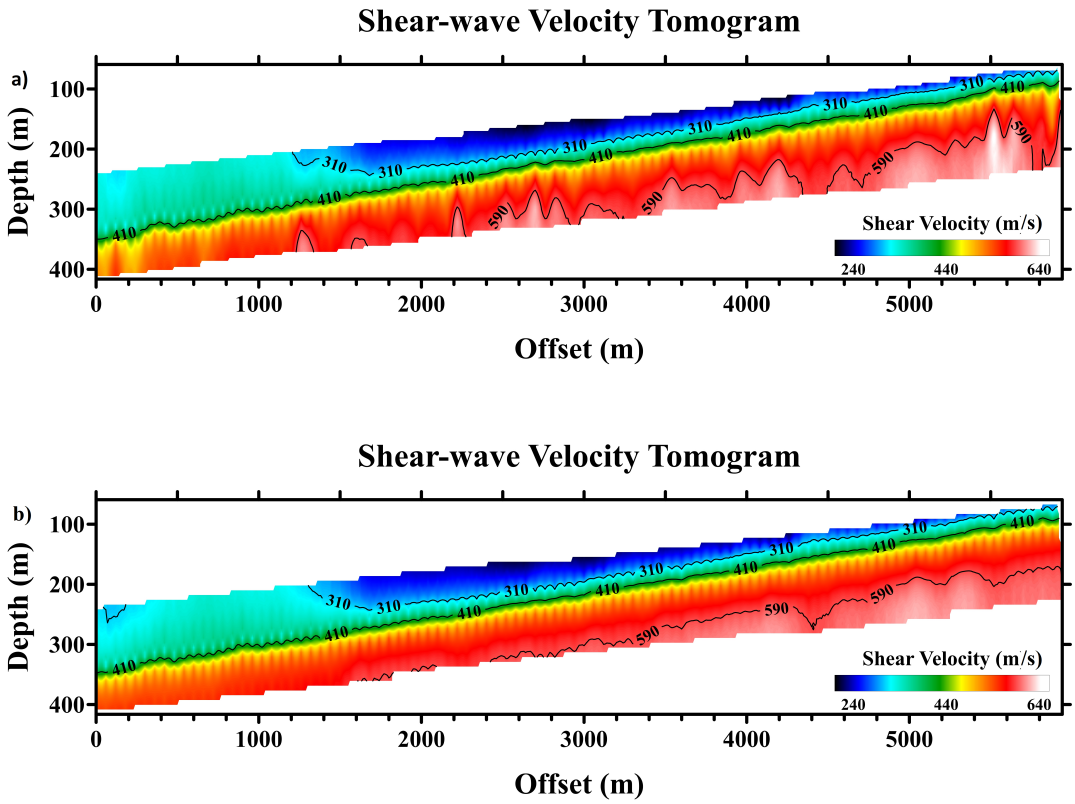

Figure 6.2.: SWT model generated from the fourth a) and fifth b) trials.

7 Discussion

The p-wave tomogram from the prior investigation will be compared with the final shear-wave velocity tomogram. We'll also check to determine if the dispersion curve disruptions play any part in this research.

7.1 Comparison of SWT and PWT

We are comparing S-wave and P-wave tomograms (figure 7.1). They should not be identical, and should not show low and high at the same locations. Usually, the shear wave will give more guesses about the geology, and the P-wave will get a bigger picture and it is smoother than the shear wave.

The good thing about this model is that it is agreeing with the sedimentary and basement part. They are complementing each other for the overall interpretation. The sedimentary part for both tomograms shows gradual thinning from west to east. It can confirm the hypothesis regarding virtual CSG which is that the sedimentary layer is not thick enough after the shot gather number 41 (from 3000 meters) to generate stronger surface waves.

The difference between SWT and PWT about the basement part is that in SWT basement seems to be thicker and thicker going from the west side to the east side, while PWT shows thinning of the basement layer. The most important thing to notice is the faults. On the PWT they can be seen very nicely, while in the SWT they cannot be confirmed. As we examined the velocities in the data, we found that the minor SWT anomaly about 4400 meters was simply fixable and hence cannot be referred to as a fault. With a shear wave analysis, there is a problem with sensitivity and going to deeper depths than a p-wave as it has better depth sensitivity. This time we thrust more PWT, because it is true 2D data, while the SWT is 1D converted into 2D.

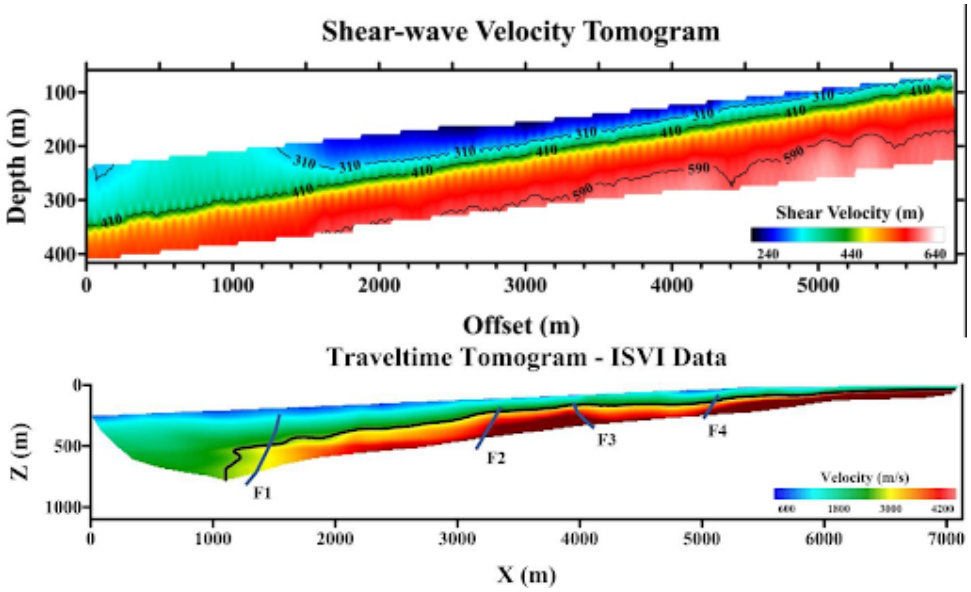

Figure 7.1.: Comparison of two tomograms, where the upper one represents our final shear-wave velocity tomogram and the lower represents traveltime tomogram from a previous study.

7.2 Dispersion curve disruptions

At first, it didn't seem of big importance, but it changed after comparing SWT with PWT. After seeing where Hanafy (2021) is predicting faults, and even if they cannot be seen on the SWT, they are matching with the noted distances where disturbances occurred (table 1).

- The first disruption (1260 - 1860 meters) occurs right where the sedimentary layer transitions into the igneous rock and where fault F1 is predicted.
- The second disruption (3120 - 3360 meters) includes fault F2.
- The third disruption (4260 - 4980 meters), on the other hand, does not include faults but rather the recess between them.
- The fourth and fifth disruptions (5280 - 5460, 5640 - 6000 meters)

For the last two disruptions, the cause may be the quick change of the layers, therefore quick change in Vs which resulted in the disruptions. On the other hand, it cannot explain the first three disruptions and it seems that maybe faults can also be a reason for the disruptions.

8 Conclusion and Recommendation

8.1 Conclusion

On a long 7.2-kilometer seismic profile we used the multichannel analysis of surface waves (MASW) technique for the analysis of the surface waves. We successfully obtained the dispersion curves that were used for the determination of a 2D shear wave tomogram which was later on, compared to a P-wave velocity tomogram.

The comparison between the shear-wave velocity tomogram (SWT) and the P-wave tomogram (PWT) reveals important insights about the subsurface structure. While they should not be identical, the two tomograms complement each other for the overall interpretation. The sedimentary layer in both tomograms shows gradual thinning from west to east, which confirms the hypothesis regarding virtual CSG.

However, there are differences between SWT and PWT. The basement portion of the SWT and PWT differ in that the SWT basement appears to be thicker traveling from the west side to the east side, whereas the PWT basement layer appears to be thinning. These are quite clearly visible on the PWT, but they cannot be verified in the SWT. We discovered that the slight SWT anomaly at a distance of 4400 meters was easily correctable when we looked at the data's velocities, therefore it cannot be referred to as a fault.

With a shear wave analysis, there is a problem with sensitivity and going to deeper depths than a p-wave as it has better depth sensitivity. This time we thrust more PWT, because it is true 2D data, while the SWT is 1D converted into 2D. Contrarily, disturbances in and around dispersion curves occurred around shot gathers where faults were anticipated (and imaged by PWT), which may be a new indicator of the existence of the fault system. These

findings provide insights into the geological structure of the NEOM area and have implications for future seismic hazard assessments.

8.2 Recommendation

This thesis is presented with a passive and active dataset, and each one of them is presented individually. As the active dataset gives very detailed information about shallower layers, and the passive can give a better overview of deeper layers, the combination of those two datasets can diminish their lack of information and enhance their valuable information. It would give a better overview of both shallow and deep layers leading to a higher resolution of seismic tomography models. A new tomographic code PARTOS can be used as it is specifically made for the joint inversion of the active and passive dataset (Alejandro Díaz-Moreno *et al.*, 2016).

Moreover, the PARTOS code gives also various possibilities for defining seismic anomalies, where one of them is the checkerboard test (Alejandro Díaz-Moreno *et al.*, 2016). The checkerboard test could be used for sensitivity analysis in a case of joint inversion for both datasets; in other words to investigate the resolution of velocity anomalies (Youssof *et al.*, 2015).

9 Bibliography

Alejandro Díaz-Moreno, Ivan Koulakov, Araceli García-Yeguas, *et al.* (Sept. 2016). „PARTOS - Passive and Active Ray TOmography Software: description and preliminary analysis using TOMO-ETNA experiment's dataset". In: *Annals of Geophysics* 59.4, p. 11.

Ben-Avraham, Zvi, Gideon Almagor, and Zvi Garfunkel (July 1979). „Sediments and structure of the Gulf of Elat (Aqaba)—Northern Red Sea". en. In: *Sedimentary Geology* 23.1-4, pp. 239–267.

Berkhout, A. J. Guus and D. J. Eric Verschuur (Feb. 2011). „A scientific framework for active and passive seismic imaging, with applications to blended data and micro-earthquake responses: Active and passive seismic imaging". en. In: *Geophysical Journal International* 184.2, pp. 777–792.

Bosworth, W., P. Montagna, E. Pons-Branchu, N. Rasul, and M. Taviani (Feb. 2017). „Seismic Hazards Implications of Uplifted Pleistocene Coral Terraces in the Gulf of Aqaba". en. In: *Scientific Reports* 7.1, p. 38.

Dal Moro, Giancarlo (2020). *Efficient joint analysis of surface waves and introduction to vibration analysis: beyond the clichés*. eng. OCLC: 1160070472. Cham: Springer.

Hanafy, S. (2019). „Iterative Super-Virtual Refraction Interferometry and Traveltime Tomography of Seismic Data: Field Example at Gulf of Aqaba". en. In: *81st EAGE Conference and Exhibition 2019*. London, UK, European Association of Geoscientists & Engineers, pp. 1–5.

Hanafy, S.M. (2022). *Personal meeting*.

Hanafy, Sherif M, M Sherif, Sigurjon Sigurjon Jonsson, and Yann Yann Klinger (2014). „Imaging normal faults in alluvial fans using geophysical techniques: Field example from the coast of Gulf of Aqaba, Saudi Arabia". In: *2014 SEG Annual Meeting*. OnePetro.

Hanafy, Sherif M. (Sept. 2021). „Active and ambient seismic data inversion: A field example from the Gulf of Aqaba". en. In: *First International Meeting for Applied Geoscience & Energy Expanded Abstracts*. Denver, CO and virtual: Society of Exploration Geophysicists, pp. 1932–1936.

Hartman, Gal, Tina M. Niemi, Gideon Tibor, Zvi Ben-Avraham, Abdallah Al-Zoubi, Yizhaq Makovsky, Emad Akawwi, Abdel-Rahman Abueladas, and Rami Al-Ruzouq (Dec. 2014). „Quaternary tectonic evolution of the Northern Gulf of Elat/Aqaba along the Dead Sea Transform: TECTONIC EVOLUTION OF THE NORTHERN GEA“. en. In: *Journal of Geophysical Research: Solid Earth* 119.12, pp. 9183–9205.

Kesarwani, Aayush, Aditi Sharma, and Chirag Jain (2012). „MASW versus refraction seismic method in terms of acquisition and processing of data and the accuracy of estimation of velocity profiles“. In: *9th Biennial International Conference & Exposition on Petroleum Geophysics, Hyderabad*. Vol. 5.

Park, Choon B., Richard D. Miller, Jianghai Xia, and Julian Ivanov (Jan. 2007). „Multichannel analysis of surface waves (MASW)—active and passive methods“. en. In: *The Leading Edge* 26.1, pp. 60–64.

Sherif M. Hanafy, Jing Li, Matt Haney, and Victor Tsai (Feb. 2020). *Written and modified MATLAB codes*.

Sherif M. Hanafy, Mohammad Youssof, and Mohamed H. Khalil (2020). „Extracting surface waves from ambient noise using interferometry: A field example“. en. In.

Al-Taani, Ahmed A., Awni Batayneh, Yousef Nazzal, Habes Ghrefat, Eslam Elawadi, and Haider Zaman (Sept. 2014). „Status of trace metals in surface seawater of the Gulf of Aqaba, Saudi Arabia“. en. In: *Marine Pollution Bulletin* 86.1-2, pp. 582–590.

Yang, Yingjie and Michael H. Ritzwoller (Feb. 2008). „Characteristics of ambient seismic noise as a source for surface wave tomography: CHARACTERISTICS OF AMBIENT SEISMIC NOISE“. en. In: *Geochemistry, Geophysics, Geosystems* 9.2, n/a–n/a.

Youssof, M., H. Thybo, I.M. Artemieva, and A. Levander (June 2015). „Upper mantle structure beneath southern African cratons from seismic finite-frequency P- and S-body wave tomography“. en. In: *Earth and Planetary Science Letters* 420, pp. 174–186.

A

Appendices

A.1 Appendix A: MATLAB Codes used for figures generation.

```
load Aqaba_Original.mat

U=data(:,42:82,42); % 42:82 is a shot gather range, 42 is chosen shot gather

[nt,ng]=size(U); %nt is number of samples, ng = num of geophones
for i=1:ng
    mx=max(abs(U(:,i)));
    if mx>0
        U(:,i)=U(:,i)/mx; % this is normalization
    end
end

%%  Input parameters
ct=100:1:1000;       % A vector for the velocity of interest in m/s.
                     % This is the velocity "scanning" range

freqlimits=[1 81];  % For plotting purposes only. Sets the frequency (Hz)
                    % plotting range for the dispersion images. Enter ['none']
                    % if you desire the natural limits based on time sampling

%%
pick='manual'; % This sets the function for picking the dispersion curve.
               % Pick setting options are 'manual' , 'auto' or 'none'

save test_Aqaba_Virt.mat
```

Figure A.1.: MATLAB codes used for easy shot gather change before dispersion curve picking, velocity “scanning” range which is for adjusting how much of a phase velocity we will see on a figure; frequency range which is one of the first parameters, chosen manual picking and how MATLAB saves the picked data.

```
7
8   ds=60;              %   Horizontal Step
9   ns=100;
10  z=100;              %   Required maximum depth
11  dz=5;               %   Vertical Step
12
13  xx=(0:ds:(ns-1)*ds)';       %   Positions of the 1D models
14  x=xx;                       %   Required x-positions
15  zz=(0:dz:z)';
16
17  nm=size(xx,1);              %   Number of 1D models
18
19  for im=1:nm
20      flnm=(['../1D_SW_Inversion_Code/Results_5th_Trial/result_',num2str(im),'.mat']);
```

Figure A.2.: MATLAB codes for 2D velocity model where ds is the distance between shot gather where it also represents a horizontal step, ns is the number of shot gathers, we chose 100 meters as a maximum depth with every 5 meters as a vertical step. As data from every dispersion curve is saved as "result_x" where x represents a number of a chosen shot gather, we are using line 20 for reading all saved results for whichever trial we want to see as a 2D velocity model.